

AD-A053 218

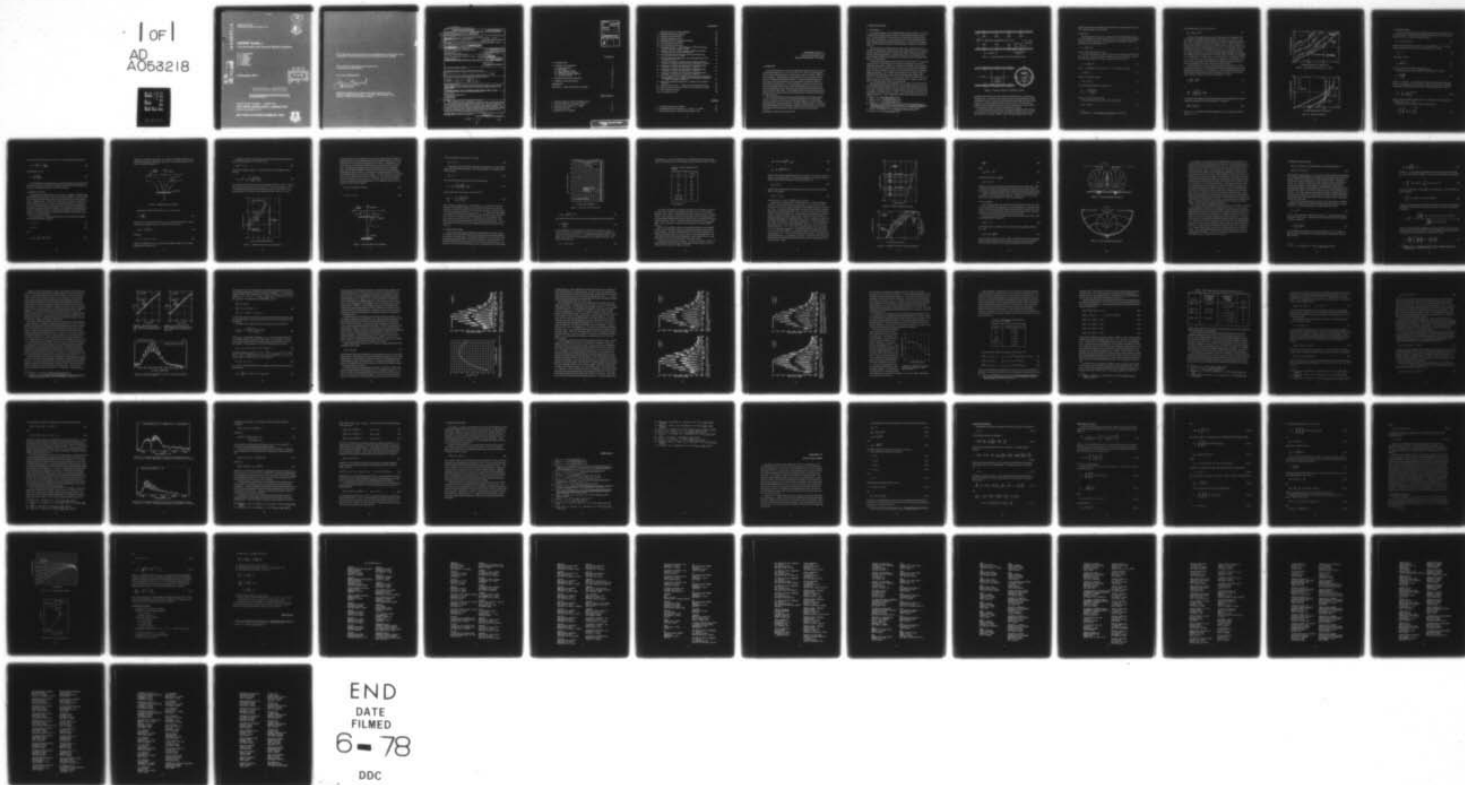
AIR FORCE GEOPHYSICS LAB HANSCOM AFB MASS
COCHISE STUDIES I: FLUID DYNAMICAL AND INFRARED SPECTRAL ANALYS--ETC(U)
DEC 77 6 E CALEDONIA, B D GREEN, G A SIMONS
AFGL-TR-77-0281

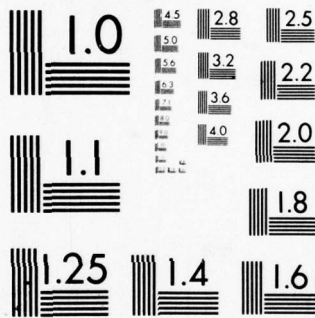
F/6 20/4

UNCLASSIFIED

NL

1 of 1
AD
A053218





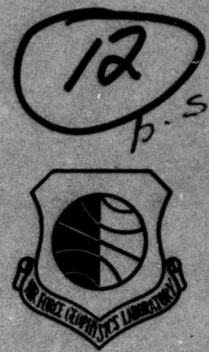
MICROCOPY RESOLUTION TEST CHART
NATIONAL BUREAU OF STANDARDS-1963-A

AD A053218

AD No.

DDC FILE COPY

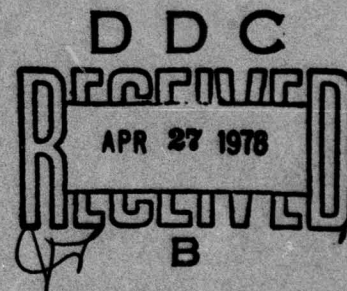
AFGL-TR-77-0281
ENVIRONMENTAL RESEARCH PAPERS, NO. 619



COCHISE Studies I: Fluid Dynamical and Infrared Spectral Analyses

G. E. CALEDONIA
B. D. GREEN
G. A. SIMONS
J. P. KENNEALY
F. X. ROBERT
A. CORMAN
F. P. DELGRECO

9 December 1977



Approved for public release; distribution unlimited.

This research was sponsored by the Defense Nuclear Agency under Subtask 125BAXHX632, Work Unit 08 entitled "IR Phenomenology and Optical Code Data Base"

OPTICAL PHYSICS DIVISION PROJECT 2310
AIR FORCE GEOPHYSICS LABORATORY
HANSCOM AFB, MASSACHUSETTS 01731

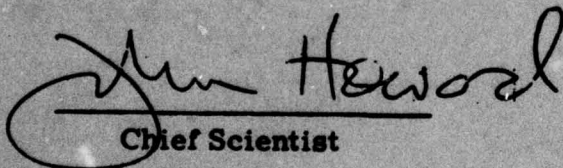
AIR FORCE SYSTEMS COMMAND, USAF



This report has been reviewed by the ESD Information Office (OI) and is releasable to the National Technical Information Service (NTIS).

This technical report has been reviewed and is approved for publication.

FOR THE COMMANDER


Chief Scientist

Qualified requestors may obtain additional copies from the Defense Documentation Center. All others should apply to the National Technical Information Service.

Unclassified

SECURITY CLASSIFICATION OF THIS PAGE (When Data Entered)

REPORT DOCUMENTATION PAGE		READ INSTRUCTIONS BEFORE COMPLETING FORM
1. REPORT NUMBER	2. GOVT ACCESSION NO.	3. RECIPIENT'S CATALOG NUMBER
14 AFGL-TR-77-0281, AFGL-ERP-619		
4. TITLE (and Subtitle)	5. TYPE OF REPORT & PERIOD COVERED	
6 COCHISE STUDIES I: FLUID DYNAMICAL AND INFRARED SPECTRAL ANALYSES.	Scientific Interim	
7. AUTHOR(s)	6. PERFORMING ORG. REPORT NUMBER	
10 G. E. Caledonia, B. D. Green, G. A. Simons, J. P. Kennealy, F. X. Robert, A. J. Gorman	ERP, No. 619	
9. PERFORMING ORGANIZATION NAME AND ADDRESS	8. CONTRACT OR GRANT NUMBER(s)	
Air Force Geophysics Laboratory (OPR) Hanscom AFB Massachusetts 01731		
11. CONTROLLING OFFICE NAME AND ADDRESS	10. PROGRAM ELEMENT, PROJECT, TASK AREA & WORK UNIT NUMBERS	
Air Force Geophysics Laboratory (OPR) Hanscom AFB Massachusetts 01731	61102F 17 G4, X632 2310G403	
14. MONITORING AGENCY NAME & ADDRESS (if different from Controlling Office)	12. REPORT DATE	
	9 Dec 1977	
	13. NUMBER OF PAGES	
	70 12 171 p.	
	15. SECURITY CLASS. (of this report)	
	Unclassified	
	15a. DECLASSIFICATION/DOWNGRADING SCHEDULE	
16. DISTRIBUTION STATEMENT (of this Report)		
Approved for public release; distribution unlimited.		
9 Environmental research papers,		
17. DISTRIBUTION STATEMENT (of the abstract entered in Block 20, if different from Report)		
16 2310, I25BAXH		
18. SUPPLEMENTARY NOTES		
This research was sponsored by the Defense Nuclear Agency under SubTask I25BAXH632, Work Unit 08 entitled "IR Phenomenology and Optical Code Data Base."		
* Physical Sciences Inc., 30 Commerce Way, Woburn, Mass. 01801		
19. KEY WORDS (Continue on reverse side if necessary and identify by block number)		
Nitric oxide Metastable nitrogen atoms Cryopumping Rarefied flow		
20. ABSTRACT (Continue on reverse side if necessary and identify by block number)		
The COCHISE facility is designed to permit the study of chemiluminescent reaction kinetics under single collision conditions. The effort reported here is concerned with the development of a detailed, fluid dynamical analysis to aid in the understanding of the flow field under experimental conditions. Preliminary results from the infrared chemiluminescent reaction of O ₂ with N(² D) atoms are analyzed, and a possible diagnostic absorption technique for the measurement of N(² D) concentrations is analyzed.		

DD FORM 1 JAN 73 1473 EDITION OF 1 NOV 65 IS OBSOLETE

Unclassified

SECURITY CLASSIFICATION OF THIS PAGE (When Data Entered)

409 578
1

st

ACCESSION for		
NTIS	White Section	<input checked="" type="checkbox"/>
DDC	Buff Section	<input type="checkbox"/>
UNANNOUNCED		<input type="checkbox"/>
JUSTIFICATION _____		
BY _____		
DISTRIBUTION/AVAILABILITY CODES		
Dist.	AVAIL and/or	SPECIAL
A		

Contents

1. INTRODUCTION	5
2. COCHISE FLUID DYNAMICS	6
2.1 System Definition	6
2.2 Inlet Tubes	8
2.3 Free Expansion Region	11
2.4 Stagnation Point - Region 3	12
2.5 Cryogenic Pumping - Region 4	16
2.6 Flow Visualization	21
3. DIAGNOSTIC AND DATA ANALYSIS	24
4. SUMMARY AND CONCLUSIONS	44
REFERENCES	45
APPENDIX A. Radial Flow Model for COCHISE	47

Illustrations

1. Schematic Diagram of AFGL COCHISE Facility	7
2. Schematic Diagram of COCHISE Flowfield	7
3. Attainable Inlet Conditions ($T_i = 100^\circ\text{K}$)	10
4. Tank Inlet Conditions	10
5. Stagnation Flow for Region 3	13

Illustrations

6. Stagnation Pressure on Tank Centerline	14
7. Newtonian Shock Layer Thickness	15
8. Pressure on Tank Centerline	17
9. Chamber Stagnation Pressure	20
10. COCHISE "Cold Wall" Operating Conditions	20
11. Flow Visualization (Top View)	22
12. Flow Visualization (End View)	22
13. Absorption of $N(3^2P - 2^2D^0)$ Radiation vs $N(^2D)$ Line Density. Lines at 1492.62 and 1492.81 Å only	27
14. Absorption of $N(3^2P - 2^2D^0)$ Radiation vs $N(^2D)$ Line Density. Lines at 1492.62, 1492.81, and 1494.67 Å	27
15. Infrared Spectra Observed in Mix of Active Nitrogen and O_2 , $P \sim 4 \times 10^{-3}$ Torr, $T \approx 100^\circ K$	27
16. Predicted Einstein Coefficients for the Fundamental Band of NO as Specified in Ref. 10	30
17. Comparison of Synthetic and Measured NO Fundamental Band Radiation; Approximate Basis Functions, Resolution = 0.013 μm	30
18. Comparison of Synthetic and Measured NO Fundamental Band Radiation; $\pi_{1/2}$ State Only, Resolution = 0.013 μm	32
19. Comparison of Synthetic and Measured NO Fundamental Band Radiation; $\pi_{1/2}$ State Only, Resolution = 0.020 μm	32
20. Comparison of Synthetic and Measured NO Fundamental Band Radiation; $\pi_{3/2}$ State Only, Resolution = 0.020 μm	33
21. Final Comparison between Synthetic and Measured NO Fundamental Band Radiation; $\pi_{1/2}$ $3/2$ States Assumed Thermally Populated at $T = 100^\circ K$, Resolution = 0.020 μm	33
22. Relative NO Vibrational Populations as Deduced from the Data of Figure 15	34
23. Observed Fluorescence from a Mix of Active Nitrogen and CO/O_2	41
24. Observed Fluorescence From a Mix of Active Nitrogen and Argon	41
A-1. Gas Temperature at Wall	54
A-2. Gas Pressure at Wall	54

Tables

1. Critical Temperature for Sticking	18
2. COCHISE Species Concentrations, $P = 4$ mtorr, $T = 100^\circ K$	35
3. Rate Constant Data for Vibrational Deactivation of NO	37

COCHISE Studies I: Fluid Dynamical and Infrared Spectral Analyses

1. INTRODUCTION

The COCHISE facility consists of a cryogenically cooled test chamber, providing operating conditions of $P \sim 10^{-3}$ torr and $T = 40 - 100^\circ\text{K}$, that was designed for the study of chemiluminescent reaction kinetics under essentially "single" collision conditions. Reactant gases are introduced into the test chamber through two sets of diametrically opposed inlet tubes. The gas entering through one of these sets can be passed through a μ -wave discharge to produce free radicals or electronically excited species. The concentrations of such species can be monitored via absorption spectroscopy. The primary diagnostic of the system is an infrared spectrometer used to monitor the spectrally resolved radiation arising from the reaction under study. The resulting radiation histories can then be interpreted in terms of reaction quantum efficiencies and the excited state distributions of reaction products.

The research conducted during the reporting period is broken into two parts: The first, described in Section 2, involved the development of a detailed fluid dynamical analysis of the flow field and operating conditions of the test chamber. The second part, described in Section 3, includes a brief examination of a proposed absorption technique for measuring the concentration of $\text{N}(^2\text{D})$ atoms, and a review and interpretation of preliminary measurements performed on the system.

(Received for publication 6 December 1977)

2. COCHISE FLUID DYNAMICS

2.1 System Definition

A schematic diagram of the COCHISE facility is shown in Figure 1. Two rows of diametrically opposed inlet jets carry the relevant chemical species into the tank. The chemical kinetics of the species are monitored in the region within 2 cm of the tank centerline. The gas then flows toward the cryogenically cooled walls which provide the necessary pumping capacity. Nominally, wall temperatures of 20°K to 40°K are expected to provide chamber pressures in the range of 10^{-3} torr.

The inlet gas flow is controlled with a needle valve. Approximately 25 cm upstream of the tank inlet, the gas pressure (p_i), temperature (T_i), and mass flow per inlet tube (M) are measured. With this information, along with the wall temperature and the tank geometry, the temperature, pressure, and density of the gas on the tank centerline can be deduced. In addition, a general flowfield visualization can be developed.

A schematic representation of the flowfield is shown in Figure 2. Top and end views and a basic recirculation cell for each jet are illustrated. Each cell is divided into four regions. Region 1 is the inlet pipe and region 2 is the expansion of the inlet flow into a relative vacuum. Region 3 is an axisymmetric stagnation point. The flow in region 2 is supersonic and must become subsonic to match the stagnation point flow. The structure surrounding region 2 is meant to depict a barrel shock and Mach disc, such as that surrounding a high altitude rocket plume¹⁻³ or free jet expansion.^{4, 5} These shocks transform a high velocity, low pressure flow into a low velocity flow of higher pressure. Region 4 is also subsonic, but the appropriate model is not yet apparent.

The total temperature at the stagnation point in region 3 is the total temperature entering the tank through the inlet jets. The stagnation pressure (p_o) in region 3 and the location of the shocks are interrelated. We must determine a value of p_{o3} that is compatible with the cryogenic pumping at the walls, then determine the location of the shocks from p_{o3} . Hence, p_{o3} is determined only from the wall capture coefficient C . These coefficients are determined empirically⁶ under the

1. Albini, F.A. (1965) AIAA Journal 3:1535.
2. Hubbard, E.W. (1966) AIAA Journal 4:1877.
3. Boynton, F.P. (1967) AIAA Journal 5:1703.
4. Ashkenas, H., and Sherman, F.S. (1966) The structure and utilization of supersonic free jets in low density wind tunnels, in Rarefied Gas Dynamics, Fourth Symposium, Vol. II. Academic Press, New York, pp. 84-105.
5. Bier, K., and Schmidt, B. (1961) Zeitschrift Agnew Physik 13:495.
6. Dawson, J.P. (1966) J. Spacecraft 3:218.

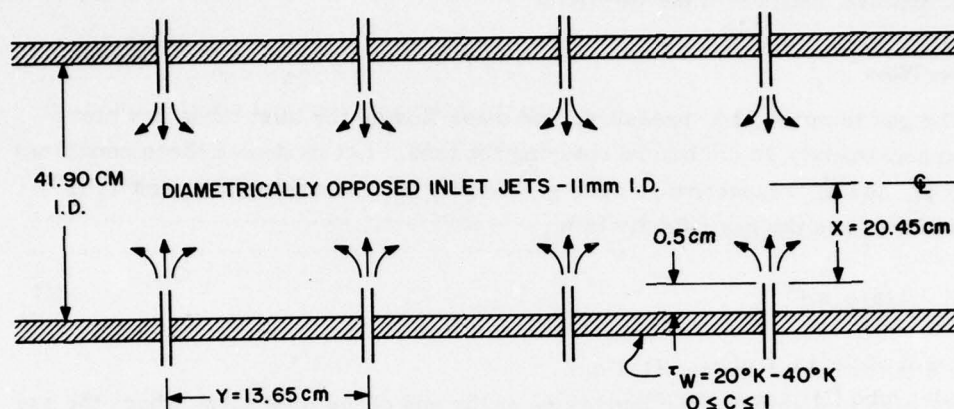


Figure 1. Schematic Diagram of AFGL COCHISE Facility

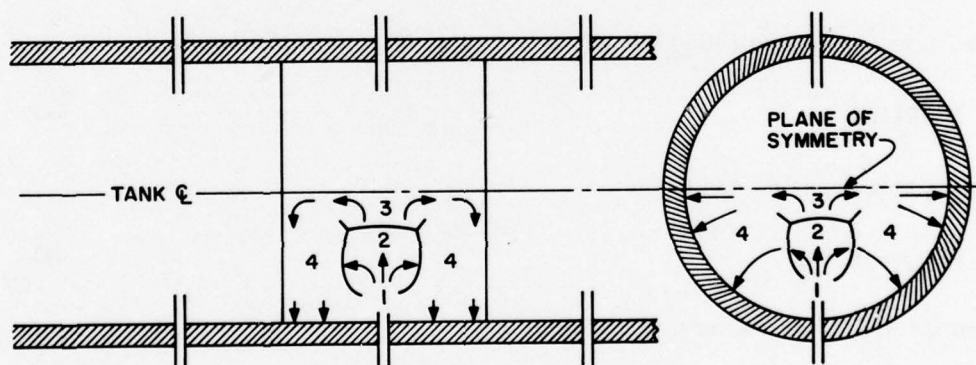


Figure 2. Schematic Diagram of COCHISE Flowfield

assumption that the gas in the tank is static with temperature T_{O_3} , pressure p_{O_3} , and density ρ_{O_3} . To develop a more detailed model for region 4 and apply capture coefficients from Ref. 6 would be inconsistent and would probably introduce extraneous errors. We shall adopt the model for region 4 that is consistent with the manner in which the capture coefficients were measured; that is, the gas is taken to be static with a uniform pressure, temperature, and density.

A more detailed model for region 4 is developed in Appendix A where the gas is shown to be a viscous continuum flow described by the Navier-Stokes equations with "slip flow" at the wall. However, this model was abandoned when it was

realized that the capture coefficients were not known accurately enough to justify such a detailed analysis of the flowfield.

2.2 Inlet Tubes

The gas temperature, pressure, and mass flow in the inlet tubes are measured approximately 25 cm before entering the tank. Let us denote these conditions as T_i , p_i , and \dot{M} , respectively. The gas density corresponding to p_i and T_i is denoted by ρ_i and the gas velocity is u_i ,

$$u_i = 4 \dot{M} / \rho_i \pi d^2, \quad (1)$$

where d is the tube diameter (1.1 cm).

We wish to determine the conditions at the end of the inlet tube, where the gas enters the tank. Let us denote these conditions with a subscript unity. The pressure drop corresponding to a laminar, incompressible pipe flow is⁷

$$p_i - p_1 = \frac{\lambda L}{2d} \rho_i u_i^2, \quad (2)$$

where L is the length of the pipe (25 cm), λ is a coefficient of friction,

$$\lambda = 64 / Re_d, \quad (3)$$

and Re_d is a Reynolds number,

$$Re_d = \rho_i u_i d / \mu_i. \quad (4)$$

From the above expressions, it follows that

$$\frac{p_1}{p_i} = 1 - \frac{128 \dot{M} \mu_i a_i^2 L}{\pi \gamma d^4 p_i^2}, \quad (5)$$

where a_i is the inlet speed of sound.

The flow Reynolds number, Re_d , may be expressed as

$$Re_d = 4 \dot{M} / \pi d \mu_i \quad (6)$$

7. Schlichting, H. (1955) Boundary Layer Theory, McGraw Hill.

and the Mach number, M_i , may be written

$$M_i = 4 \dot{M} a_i / \gamma \pi p_i d^2 \quad (7)$$

Equations (5) through (7) impose three constraints on the combinations of \dot{M} and p_i that are compatible with the inlet pipe. We require $p_i \geq 0$, $M_i \leq 1$, and $Re_d \leq 2300$. The Reynolds number constraint is imposed to prevent turbulent pipe flow. These constraints are illustrated in Figure 3 for $T_i = 100^\circ K$. Clearly we should keep our pressure losses to less than 10 percent to avoid significant viscous heating of the inlet gas. Maintaining $p_i \geq 0.9 p_1$, $M_i < 0.25$, and $Re_d < 2300$, we can be sure that p_i and T_i are within 10 percent of our measurements of p_1 and T_i . Figure 4 illustrates the conditions under which these constraints are satisfied. The calculations were carried out for $T_i = 300^\circ K$, $100^\circ K$, and $60^\circ K$, corresponding to $a_i = 30,000$ cm/sec, $17,000$ cm/sec, and $13,000$ cm/sec, respectively, and for $\mu_i = 2 \times 10^{-4}$, 10^{-4} , and 6×10^{-5} gm/cm-sec, respectively. If a pressure of 5 to 10 torr can be maintained in the inlet pipe, the conditions measured in the inlet tube are equivalent to those under which the gas enters the tank.

In the event that the 5 to 10 torr pressure cannot be maintained, the viscous losses will heat the gas. This heating can be offset by maintaining the walls of the inlet pipes at temperature T_i . The question is, how hot will the gas become before the dissipation will be balanced by heat conduction to the wall? Let us seek the final state where conduction does balance dissipation. We write

$$C_p \frac{\partial^2 T}{\partial r^2} = \left(\frac{\partial u}{\partial r} \right)^2 \quad (8)$$

or

$$\frac{\Delta T}{T_i} = O \left(\frac{u_i^2}{C_p T_i} \right) = O(M_i^2) \quad (9)$$

To determine the constant in the above relationship, we acknowledge that viscosity cannot heat the gas above the total temperature. Therefore,

$$\frac{\Delta T}{T_i} \leq \frac{\gamma - 1}{2} M_i^2 \quad (10)$$

Since $M_i \leq 1$, the maximum possible temperature rise in the inlet tube is 20 percent for $\gamma = 1.4$.

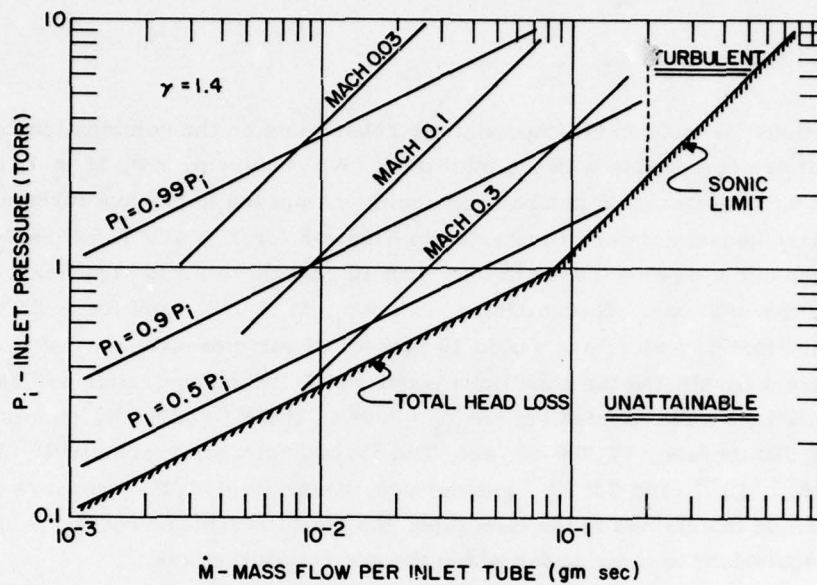


Figure 3. Attainable Inlet Conditions ($T_i = 100^\circ\text{K}$)

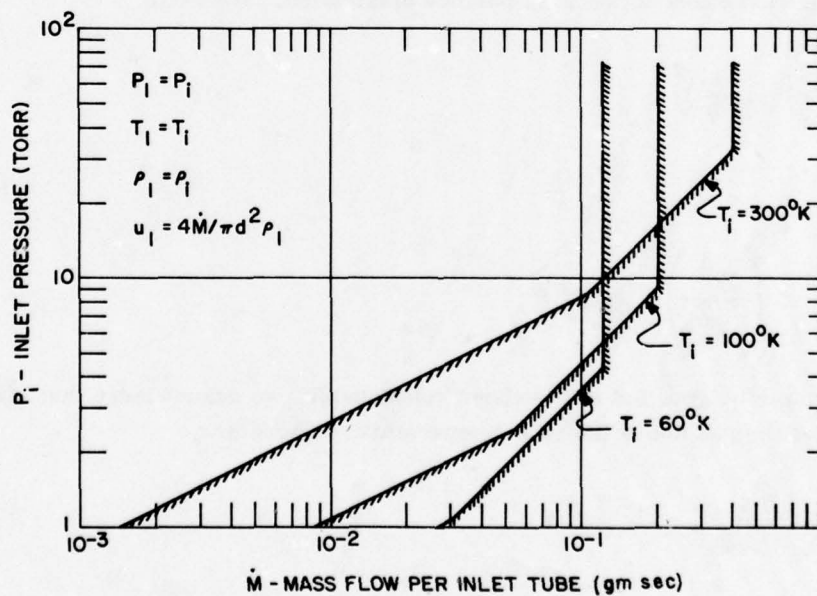


Figure 4. Tank Inlet Conditions

2.3 Free Expansion Region

The flow within the barrel shock and Mach disc expands as though there were no back pressure. The gas reaches a limiting velocity in which all of the thermal energy of the flow is converted into kinetic energy,

$$u_2 = (u_1^2 + 2 C_p T_1)^{1/2} \quad (11)$$

Since the inlet Mach number is subsonic, it follows that $M_1^2 \ll 2/(\gamma - 1)$ and the stagnation temperature in the free jet is approximately T_i . Hence,

$$T_{o2} = T_i \quad (12)$$

from which we obtain

$$u_2 = \sqrt{\frac{2}{\gamma - 1}} a_i \quad (13)$$

where a_i is the speed of sound corresponding to T_i .

The gas density in the free expansion is approximately^{3,4} given by

$$\rho_2 = \frac{A f(\theta) \dot{M}}{u_2 r_2^2} \quad (14)$$

where A is a constant, r_2 is the spherical radius from the exit plane of the inlet tube, θ is measured from the jet centerline, and $f(\theta)$ is obtained from numerical calculations of high altitude rocket plumes. A good approximation for $f(\theta)$ is³

$$f(\theta) = \left[\cos \left(\frac{\pi \theta}{2 \theta_\infty} \right) \right]^{2/(\gamma-1)} \quad (15)$$

where θ_∞ is the maximum turning angle for the expansion of an isentropic gas to a vacuum (130.6° for $\gamma = 1.4$).

Conservation of mass requires that A be determined by

$$A = \left[2 \int_0^{\theta_\infty} f(\theta) \sin \theta d\theta \right]^{-1} \quad (16)$$

Since most of the mass flux occurs near $\theta = 0$, we approximate the sine of θ by

$$\sin \theta \approx \frac{2\theta_{\infty}}{\pi} \sin \left(\frac{\pi \theta}{2\theta_{\infty}} \right), \quad (17)$$

and determine A to be

$$A = \frac{(\gamma + 1)\pi}{8(\gamma - 1)\theta_{\infty}^2}. \quad (18)$$

The expressions for the gas velocity u_2 and the gas density ρ_2 are valid within the shock structure. The location of the shock structure must be determined as a function of the stagnation pressure on the tank centerline.

2.4 Stagnation Point - Region 3

The diametrically opposed inlet jets will interact in a plane of symmetry passing through the tank centerline. This was illustrated in Figure 2. Symmetry about the jet centerline indicates that the flow may be modeled as an inviscid, axisymmetric, stagnation point. Furthermore, in passing from region 2 to region 3, the flow on the jet centerline must traverse a plane normal shock wave. Hence, the flow in the stagnation region is subsonic and may be treated as incompressible. In addition to the incompressible assumption, we assume that the stagnation point solution is equivalent to that for which the flow is initially normal to the plane of symmetry. This approximation is strictly valid only on the jet centerline, where regions 2 and 3 will be matched.

The incompressible, potential flow solution for the axisymmetric stagnation point as described above is given by⁷

$$u_3 = 2mz, \quad (19)$$

$$w_3 = mr_3, \quad (20)$$

and

$$p_3 = p_{o3} - \frac{\rho_3}{2} m^2 (r_3^2 + 4z^2), \quad (21)$$

where m is a constant of the motion, u_3 is normal to the plane of symmetry, w_3 is parallel to the plane of symmetry, and r_3 and z are the axisymmetric coordinates, as indicated in Figure 5.

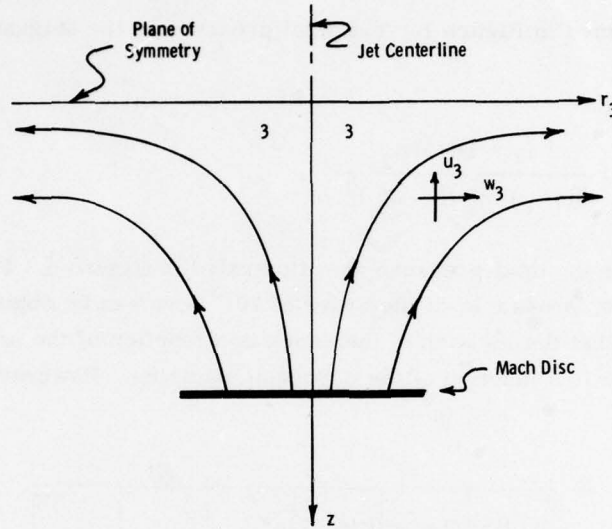


Figure 5. Stagnation Flow for Region 3

Denoting the location of the shock by $z = Z_s$, we note that

$$m = \frac{u_3(Z_s)}{2 Z_s} , \quad (22)$$

where $u_3(Z_s)$ is the post shock value of u_2 . For strong shocks (which is compatible with the assumption that u_2 is a limiting velocity), we write

$$u_3(Z_s) = \left(\frac{\gamma - 1}{\gamma + 1} \right) u_2 . \quad (23)$$

Therefore,

$$m = (\gamma - 1) u_2 / 2 (\gamma + 1) Z_s , \quad (24)$$

where Z_s is unknown and must be determined through knowledge of the cryogenic pumping at the chamber walls.

Denoting the distance from the exit plane of the inlet tube to the Mach disc by $R_s(\theta)$, we note that $R_s(\theta = 0)$ is related to Z_s by

$$R_s(0) = X - Z_s, \quad (25)$$

where X was defined in Figure 1. The total pressure in the stagnation region becomes

$$p_{O_3} = \rho_2 u_2^2 = \frac{(\gamma + 1) \pi \dot{M} u_2}{8(\gamma - 1) \theta_\infty^2 (X - Z_s)^2} \quad (26)$$

These results for the total pressure are illustrated in Figure 6. For $\dot{M} = 0.03$ gm/sec per inlet tube, pressures of the order of 10^{-3} torr can be obtained. It must be remembered that the location of the shock is a function of the pressure, p_{O_3} , and that pressure is a function of the cryogenic pumping. However, Z_s is an

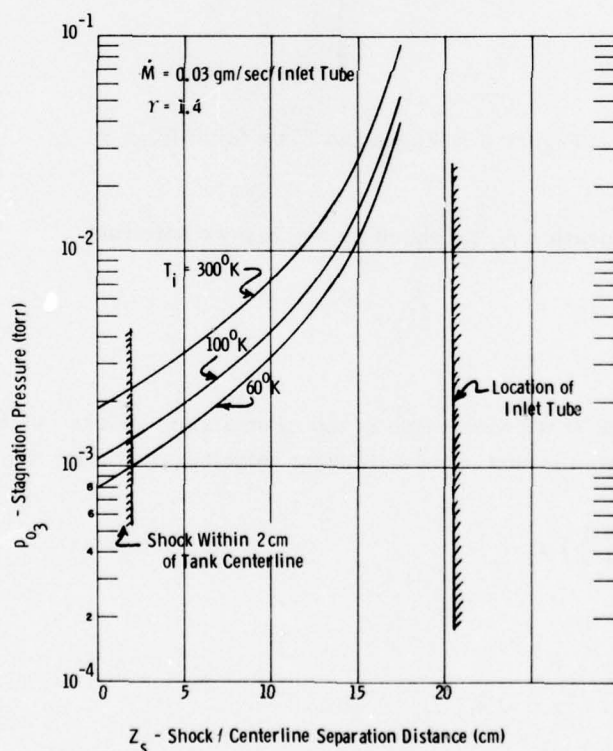


Figure 6. Stagnation Pressure on Tank Centerline

important parameter in the analysis, because we must keep the shock a couple of centimeters away from the tank centerline to ensure that the optical monitor of the experiment does not see the underexpanded flow of region 2. Physically, Z_s cannot become zero since continuity requires that some minimum value of Z_s must exist. Raising the background pressure could increase Z_s above its minimum value, but lowering the background pressure would result in Z_s monotonically approaching a minimum value to be determined by a Newtonian pressure balance. The Newtonian balance is illustrated in Figure 7. The inlet tube acts as a spherical source that is reflected from the plane of symmetry. The component of velocity normal to the plane of symmetry is lost to pressure, but $u_2 \sin \theta$ is conserved across the shock and moves the high pressure, low velocity gas lateral to the jet centerline. Mass balance suggests

$$\rho_2 u_2 \pi r_2^2 = (6\rho_2)(u_2 \sin \theta) 2\pi r_2 \delta \quad (27)$$

or

$$\delta = X/12 = 1.7 \text{ cm} \quad (28)$$

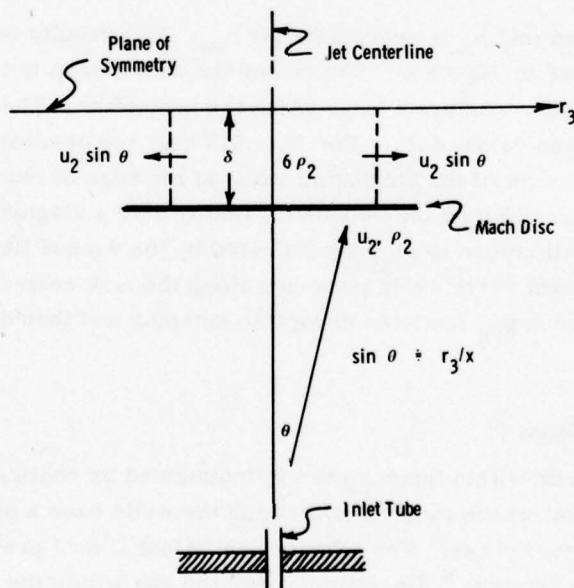


Figure 7. Newtonian Shock Layer Thickness

Thus, the minimum value of Z_s is 1.7 cm and

$$Z_s \geq 1.7 \text{ cm} \quad (29)$$

To determine the static pressure along the tank centerline, we require knowledge of the temperature and density. The total temperature is conserved across the shock wave,

$$T_{O_3} = T_i \quad (30)$$

The total pressure and temperature yield the total density,

$$\rho_{O_3} = \frac{\gamma(\gamma + 1) \pi \dot{M}}{4(\gamma - 1)^2 u_2 \theta_\infty^2 (X - Z_s)^2} \quad (31)$$

and the expression for the static pressure becomes

$$\frac{p_3}{p_{O_3}} = 1 - \frac{\gamma(\gamma - 1)(r_3^2 + 4z^2)}{4(\gamma + 1)^2 Z_s^2} \quad (32)$$

where we have assumed that ρ_3 is approximately ρ_{O_3} . The results for the static pressure are illustrated in Figure 8. The closer the shock wave is to the tank centerline, the faster the pressure decays along the centerline. The fastest decay occurs for the Newtonian value of Z_s . For $Z_s = 1.7$ cm, the pressure would decay to a minimum of 60 percent of the stagnation value at the edge of the recirculation zone. However, this position on the tank centerline is also a stagnation point. The static pressure will return to p_{O_3} , as indicated by the dashed lines. Hence, there is only a 10 percent variation in pressure along the tank centerline. We will now proceed to determine p_{O_3} from the cryogenic pumping and then determine Z_s from p_{O_3} .

2.5 Cryogenic Pumping - Region 4

The relative vacuum within the chamber is maintained by cooling the walls of the chamber to the point where molecules striking the walls have a high probability of sticking in a condensed phase. The capture coefficient C for "pre-frosted" walls has been measured by Dawson.⁶ He assumes that the gas within the chamber is a stationary Maxwellian gas of temperature T_i , pressure p_{O_3} , and density ρ_{O_3} . The maximum mass flux toward the wall per unit area is determined from kinetic theory:

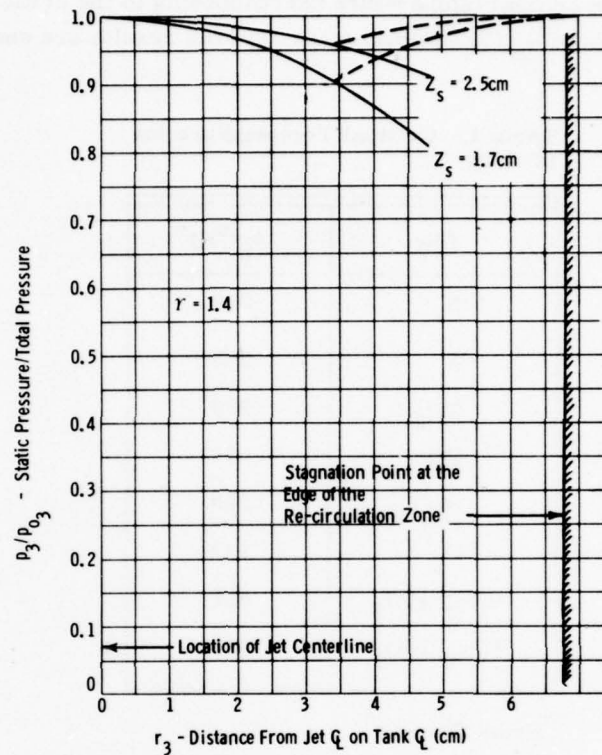


Figure 8. Pressure on Tank Centerline

$$\dot{m}_{\max} = \sqrt{\gamma/2\pi} p_{O_3}/a_i \quad (33)$$

The actual mass flux toward the wall is used to define the capture coefficient C ,

$$C = \frac{\dot{m}_{\text{actual}}}{\dot{m}_{\max}} \quad (34)$$

A theoretical basis for determining C is called the critical velocity model. It states that there is some maximum normal velocity with which a molecule can strike a pre-frosted wall and stick. In a Maxwellian distribution function, there always exist some fraction of the molecules that are capable of sticking. That fraction is denoted by C :

$$C = 1 - \exp(-\tau_c/T_i) \quad (35)$$

The quantity τ_c is a critical temperature corresponding to the critical velocity. Dawson⁶ has measured τ_c for various gases, and his results are shown in Table 1.

Table 1. Critical Temperature for Sticking

Gas	$\tau_c (^{\circ}\text{K})^*$
N ₂	290
A	293
CO ₂	289
CO	532
N ₂ O	288
O ₂	532
90N ₂ /10O ₂	361
80N ₂ /20O ₂	416

*From Dawson⁶

In reality, the behaviour of the gas in the tank is not as idealistic as Dawson assumed. Once molecules are captured at the wall, there is a mean velocity toward the wall. Hence, the Maxwellian distribution function near the wall should include a mean velocity u_w , and a gas temperature T_w that is different from T_i . This distribution function would yield a smaller fraction of molecules with normal velocity less than "critical." In addition, the basic expression for \dot{m}_{\max} would differ. Hence, the capture coefficient would be different from those given by Dawson.

While it is "desirable" to give a more detailed description of the COCHISE facility, one does not know the capture coefficients accurately enough to justify such an analysis. The most realistic approach is to use the model that was assumed in the measurements of C, that is, that of a static Maxwellian gas. The more detailed model is described in Appendix A and most likely will not be used unless there are some gross inadequacies in the static model.

Using the same assumption as Dawson, we conserve mass flux. That is, the mass flowing into the tank through two opposing jets must be captured over the wall area $2\pi RY$, where R is radius of the tank:

$$2 \dot{M} = C(2 \pi R Y) \sqrt{\gamma/2\pi} p_{O_3}/a_i \quad (36)$$

or

$$p_{O_3} = \dot{M} a_i \sqrt{2/\pi\gamma}/C R Y \quad (37)$$

Equation (37) yields the stagnation pressure as a function of mass flow, inlet temperature, and tank geometry. The primary constraint on p_{O_3} is that it must be in excess of the gas vapor pressure at the wall temperature τ_w ,

$$p_{O_3} \geq p_v(\tau_w) \quad (38)$$

otherwise the condensed phase would vaporize and raise the pressure within the tank. For most gases

$$\ln p_v = A - B/\tau_w \quad (39)$$

where, for N_2 , $A = 16.9$, $B = 800^\circ K$, and p_v is in torr.

Equations (37) and (39) yield the initial predictions for the tank centerline pressure. Figure 9 illustrates p_{O_3} as a function of τ_w , T_i , and \dot{M} . The wall temperature is assumed to have no influence on the stagnation pressure, provided $p_{O_3} > 10 p_v$. For larger wall temperatures, the pressure is assumed to increase and follow the vapor pressure curve. The "cold wall" results are illustrated as a function of mass flow in Figure 10. The maximum wall temperature for which the results are valid is indicated. There is also an upper limit on \dot{M} for each T_i to prevent the inlet pipe from becoming turbulent. This is so indicated in Figure 10, as obtained from Figure 4. Each value of T_i possesses, within the framework of this model, a unique value of shock stand-off distance, Z_s . This is obtained from Eqs. (26) and (37). For T_i of $100^\circ K$ and $60^\circ K$, this value of Z_s falls below the Newtonian limit of 1.7 cm. Hence, the corresponding value of Z_s is corrected to 1.7 cm, as indicated in Figure 10. The additional constraint expressed in Figure 10 is a gross approximation to the effect of diffusion from the wall to the tank centerline. If, at $t = 0$, we "turn on" the diffusion at the wall, it will diffuse with velocity $\sqrt{\nu/t}$ where ν is the kinematic viscosity. The diffusion front will propagate toward the tank centerline until the diffusion velocity is just balanced by the mean velocity u . Hence,

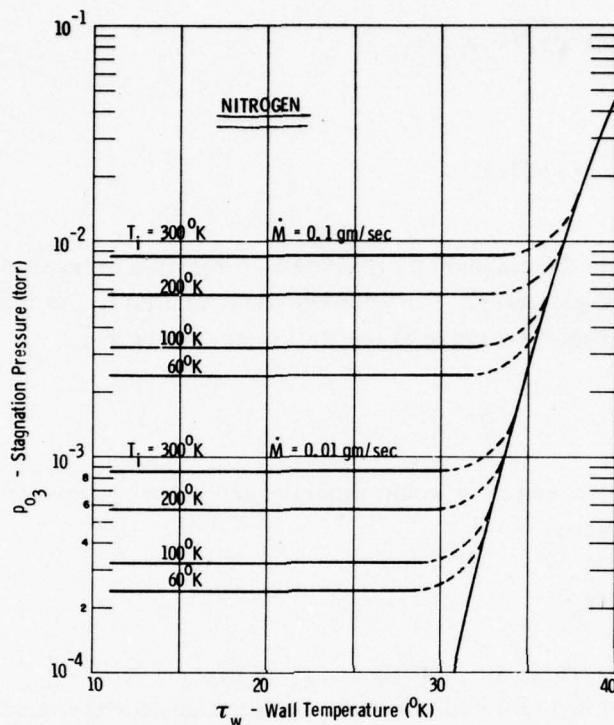


Figure 9. Chamber Stagnation Pressure

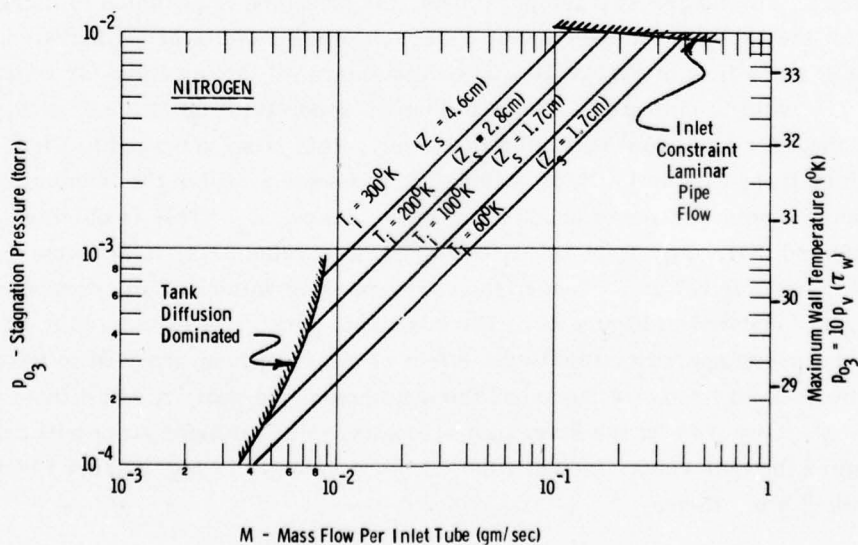


Figure 10. COCHISE "Cold Wall" Operating Conditions

$$\sqrt{\frac{\nu}{t}} = u \quad (40)$$

where

$$\rho_{O_3} u^2 \pi R Y = 2 \dot{M} \quad (41)$$

The diffusion distance Δ is $\sqrt{\nu t}$ or

$$\Delta/R = \mu \pi Y / \dot{M} \quad (42)$$

Diffusion from the wall will affect the centerline when Δ/R is order unity. This is so indicated in Figure 10 and represents a minimum mass flux under which the tank can operate without contamination of the tank centerline by the chamber walls.

Figure 10 represents the major result of this study: tank centerline pressure as a function of the measured input conditions. Upper and lower bounds on the mass flow for which the analysis is valid are also indicated.

2.6 Flow Visualization

The preceding analysis has predicted the tank centerline pressures as a function of the mass flow, gas temperature, and wall temperature. The analysis also predicts the location of the shock waves with respect to the tank centerline. What remains is a scale drawing of the shock structure within the tank and a visualization of how the gas flows through the shocks and to the walls.

The location of the shock from the exit plane of the inlet tube on the jet centerline was determined in Section 2.4,

$$R_s(0) = X - Z_s \quad (25)$$

To determine $R_s(\theta)$, we find the locus of points such that $\rho_2(\theta) u_2^2$ is identical to ρ_{O_3} . Thus,

$$R_s(\theta) = R_s(0) \sqrt{f(\theta)} \quad (43)$$

$R_s(\theta)$ is shown in Figures 11 and 12. Figure 11 shows that the free jet expansions actually impinge and minimize the flow along the axis of the tank, and Figure 12 shows that the dominant flow is in the plane perpendicular to the tank axis.

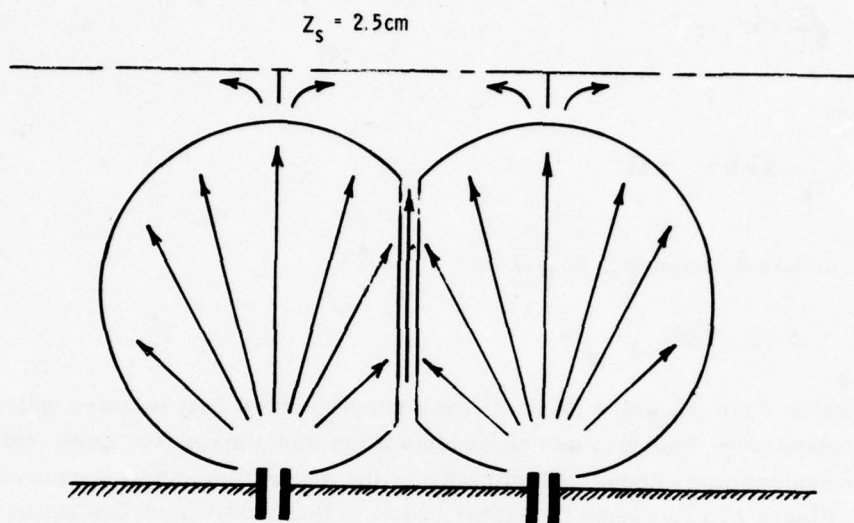


Figure 11. Flow Visualization (Top View)

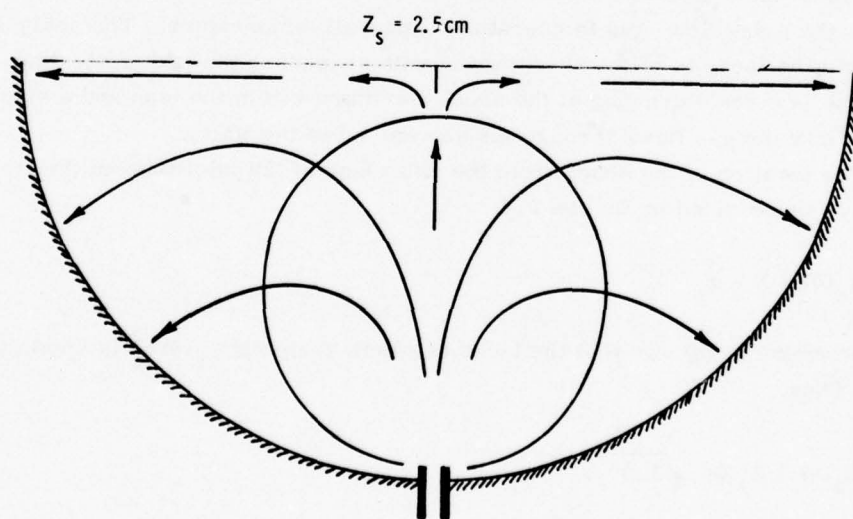


Figure 12. Flow Visualization (End View)

In conclusion, a description of the COCHISE facility has been provided. Of primary interest was the determination of the pressure on the tank centerline as a function of the inlet temperature and mass flow rate. The inlet temperature and pressures are measured at a location in the inlet tube approximately 25 cm upstream of the tank. Figure 4 was constructed to determine the conditions under which these measurements were meaningful representations of the properties of the gas where it flows into the tank. Gas temperatures could increase as much as 20 percent if the constraints of Figure 4 are not obeyed. An analysis of the flow on the tank centerline illustrates that the centerline pressure is within 10 percent of being uniform along the axis of the tank. Shock waves do exist within the tank and come within 1.7 cm of the tank centerline. This distance increases to above 2.5 cm when the gas inlet temperature is raised above 200°K. The predictions for the centerline pressure are given in Figure 10. For any inlet temperature T_i , there exists a maximum mass flow per inlet tube for which the flow in the inlet tube is laminar. Higher mass flows would introduce turbulent pipe flow, and its effect has not been assessed. There exists a minimum mass flow, below which diffusion from the chamber walls may affect the tank centerline. This effect need not necessarily be detrimental to the facility. The constraint merely indicates the onset of the phenomenon and a detailed analysis would be required to examine it further. Such a model is discussed in Appendix A.

The present results are applicable only for the case of a "cold wall." Raising the wall temperature would allow the condensed gas to vaporize. The maximum wall temperature for which the present analysis is valid is also shown in Figure 10. Within these constraints, the present analysis predicts the chamber pressure as a function of mass flow and gas temperature. A possible source of error in the prediction will lie in the "static gas" approximation made in Section 2.5. From the mass flow rates, we determine that the Mach number at the wall is approximately 1/3. This has a direct effect on pressure of only 10 percent. The cooling of the gas in the vicinity of the wall should have a direct effect on the capture coefficient. However, this effect should be incorporated in Dawson's data⁶ of C as a function of T_i . Hence, using the same model as Dawson should yield the most accurate results. The above prediction should yield 10 percent accuracy due to the static incompressible assumption. Since the incompressible assumption was made in both regions 3 and 4, 20 percent errors may result.

3. DIAGNOSTIC AND DATA ANALYSIS

One of the reactions of primary interest to the COCHISE program is



Reaction (44) is exothermic by ≈ 3.6 eV, and it is desired to determine the fraction of the reaction exothermicity that is channeled to NO vibrational energy as well as the rate constants for creating NO in various vibrational levels. The species $\text{N}(^2\text{D})$ may be created by passing N_2 or a mix of N_2/Ar through a microwave discharge. It is proposed to measure the $\text{N}(^2\text{D})$ concentration via absorption of nitrogen lamp radiation, as described by Lin and Kaufman.⁸ There are three strong nitrogen-emission lines arising from $\text{N}(3\text{S}^2\text{P}) \rightarrow \text{N}(^2\text{D}^0)$ transitions, occurring at 1492.62, 1492.81, and 1494.67 Å, that can be used in the absorption measurement. Since optical filtering requirements are greatly simplified if all three of these lines can be monitored, it was desirable to specify the relative $\text{N}(^2\text{D})$ detection efficiency when monitoring all three lines as compared to that for monitoring just the two closest lines.

Such a determination involves the evaluation of the transmission of a Doppler-broadened lamp line through a Doppler-broadened absorption medium at a lower temperature. A Doppler lineshape may be described by the formula

$$k_v = k_o e^{-w^2} \quad (45)$$

where k_v is the absorption coefficient at frequency v , k_o is the absorption coefficient at line center, and w , which contains the lineshape behavior with frequency variation, is defined by

$$w = \frac{(v - v_o)}{b_D} \sqrt{\ln 2} \quad ; \quad (46)$$

b_D , the Doppler line halfwidth, is directly proportional to \sqrt{T} . The higher temperature emission lineshape and the resonant absorption lineshape for a gas are then related by

8. Lin, C. L., and Kaufman, F. (1971) J. Chem. Phys. 55:3760.

$$w_a = w_e \sqrt{\frac{T_e}{T_a}} = w_e \alpha \quad (47)$$

Because $\alpha > 1$, the absorption lineshape falls off more rapidly with increasing $(\nu - \nu_0)$ than the emission lineshape. The lamp line emission may be represented by

$$I_o = \int_{-\infty}^{\infty} C \exp(-w_e^2) dw = \int_{-\infty}^{\infty} C \exp(-w_a^2/\alpha^2) dw \quad (48)$$

where C is proportional to the strength of the emitting line. The transmitted radiation is given by

$$I = \int_{-\infty}^{\infty} C \exp(-w_e^2) \exp(-k_o N \ell \exp(-w_a^2)) dw \quad (49)$$

where N is the concentration of absorbers (molecules/cm³) and ℓ is the absorption path length. Thus the fraction of emitted energy lost to resonant self absorption is defined by

$$A_\alpha = \frac{I_o - I}{I_o} = 1 - \frac{\int_{-\infty}^{\infty} \sum_{i=1}^3 C_i \exp(-w_i^2/\alpha^2) \exp[-k_{o,i} N \ell \exp(-w_i^2)] dw_i}{\int_{-\infty}^{\infty} \sum_{i=1}^3 C_i \exp(-w_i^2/\alpha^2) dw_i} \quad (50)$$

where w is for the absorption lineshape, and the summation is over the three previously defined lines that are taken to be non-overlapping.⁸ Equation (50) may be represented as a series expansion for small values of $k_o N \ell$:⁹

$$A_\alpha = \left(\sum_{i=1}^3 C_i \right)^{-1} \sum_{j=0}^{\infty} \sum_{i=1}^3 (-1)^{j-1} \frac{C_i (k_{o,i} N \ell)^j}{j! (j\alpha^2 + 1)^{1/2}} \quad (51)$$

9. Mitchell, A.C.G., and Zemansky, M.W. (1934) Resonance Radiation and Excited Atoms, Cambridge, London, p 323.

Equation (51) has been evaluated as a function of absorber line density for the three lines in question using the line strengths, degeneracies, etc., provided in Ref. 8. The predicted absorption histories for the cases of lines at 1492.62 and 1492.81 Å only, and for all three lines are shown in Figures 13 and 14, respectively. These predictions are nominally for a lamp temperature of 600°K and absorbing gas temperatures from 40 to 600°K, but the predictions are approximately valid for other lamp and absorber temperatures exhibiting the same temperature ratio α . From a comparison of Figures 13 and 14, it can be seen that the inclusion of the transition at 1494.67 Å causes only a slight decrease in diagnostic sensitivity. The relevant path length of the COCHISE facility is 100 cm; thus, $N(^2D)$ concentrations of $10^9/\text{cm}^3$ could be monitored if 1 percent changes in lamp intensity can be detected. Lastly, the variation of absorptance with absorber temperature can be seen to be relatively weak, the absorptance changing by less than 30 percent for a factor of 15 change in temperature.

Although the $N(^2D)$ diagnostic has not yet been implemented on the COCHISE facility, a number of preliminary studies have been performed. The first of these involved a measurement of the infrared chemiluminescence arising from reaction (44). In this experiment a mixture of 10 percent N_2 /90 percent Ar was passed through a microwave discharge and then mixed in the test chamber with oxygen. Chamber conditions were estimated to be $P = 4 \times 10^{-3}$ torr, $T = 100^\circ\text{K}$. A portion of the spectra observed in this mix is shown in Figure 15. The dominant feature of the data is radiation from the NO fundamental vibration/rotation band whose $v = 1 \rightarrow 0$ band origin is at 5.33 μm . There is also some radiation from an unknown source observed at lower wavelengths, 5.03–5.23 μm , as can be seen in Figure 15.

The first step in the analysis of this data is to deduce the relative vibrational level populations of NO corresponding to this spectra. Because the vibrational distributions are non-Boltzmann, this step requires an iterative comparison between the data and an artificially generated spectrum. This spectrum is synthesized from normalized "basis functions," $\xi_v(\nu)$ (where ν is in wavenumbers) which are the spectral bands arising from the individual vibrational transitions, $v \rightarrow v - 1$.

The NO electronic ground-state has one quantum of orbital angular momentum, l (and thus is a π state), and also exhibits spin angular momentum from an unpaired electron. It has been determined¹⁰ that in NO the coupling of the spin and orbital angular momentum is very strong (Hund's coupling, case a)¹¹ and remains strong for all rotational levels populated in the present experiment. Thus, two total angular momentum (Ω) states are allowed, $\Omega = 1/2$ and $3/2$. Coupling between Ω

10. Billingsley, F. P. (1976) *J. Molecular Spectroscopy* 61:53.

11. Herzberg, G. (1951) *Molecular Spectra and Molecular Structure I, Spectra of Diatomic Molecules*, 2nd ed., D. Van Nostrand Co., New York.

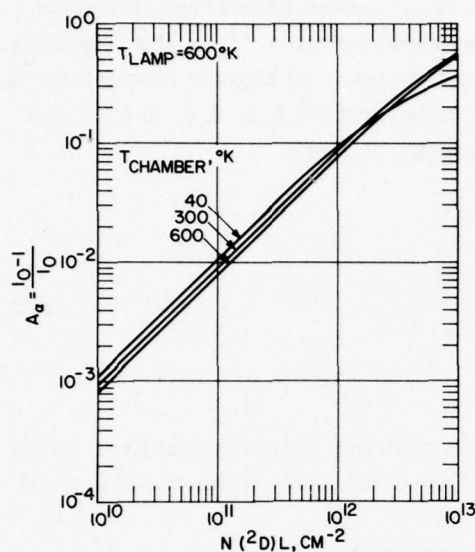


Figure 13. Absorption of $N(3^2P - 2^2D^0)$ Radiation vs $N(2D)$ Line Density. Lines at 1492.62 and 1492.81 Å only

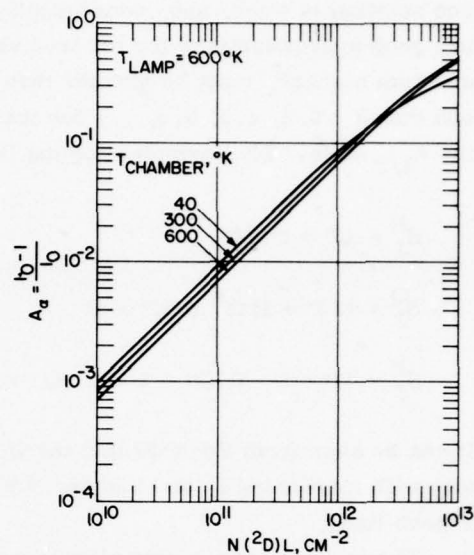


Figure 14. Absorption of $N(3^2P - 2^2D^0)$ Radiation vs $N(2D)$ Line Density. Lines at 1492.62, 1492.81, and 1494.67 Å

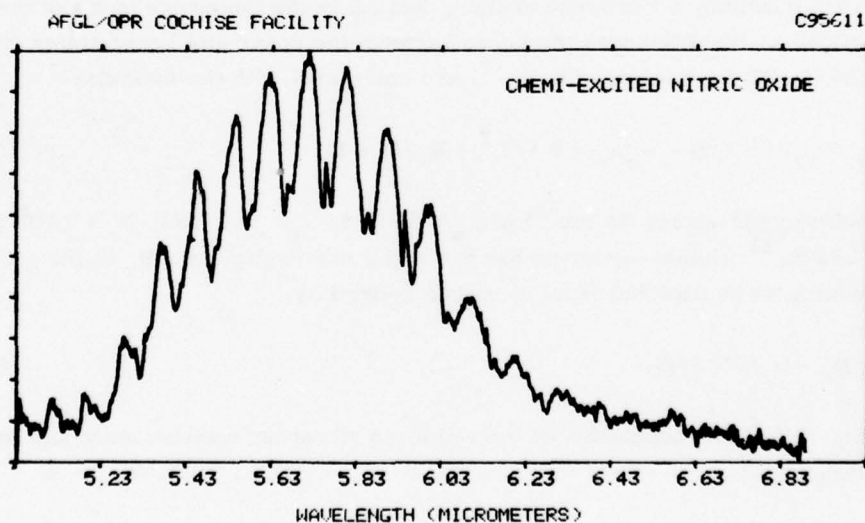


Figure 15. Infrared Spectra Observed in Mix of Active Nitrogen and O_2 , $P \sim 4 \times 10^{-3}$ Torr, $T \approx 100^\circ K$

and rotation is weak, and, consequently, the Hönl-London linestrength formulas are good approximations for the true rotational linestrengths.¹¹ J , the rotational quantum number, must be greater than or equal to the total angular momentum, Ω , and thus $J = 0.5, 1.5, 2.5, \dots$ for the $\pi_{1/2}$ state, and $J = 1.5, 2.5, 3.5, \dots$ for the $\pi_{3/2}$ state. The formulas for the linestrength, S_J , are:

$$\begin{aligned} S_J^R &= (J' + \Omega)/J' \\ S_J^Q &= (2J' + 1)\Omega^2/J'(J' + 1) \\ S_J^P &= (J' + 1 + \Omega)(J' + 1 - \Omega)/(J' + 1) \end{aligned} \quad (52)$$

It can be seen from Eq. (52) that the Q branch lines will diminish rapidly in intensity with increasing J , and that the P branch lines will be more intense than the R branch lines.

The intensity of a single vibration/rotation transition is specified by:¹¹

$$I_{J \rightarrow J, J \pm 1}^{v \rightarrow v-1} = \frac{hc \nu_T^4 S_J^{P, Q, R} A_{v \rightarrow v-1} N_{v, J}}{(2J + 1) \nu_{v \rightarrow v-1}^3}, \quad (53)$$

where $A_{v \rightarrow v-1}$ is the Einstein coefficient, $\nu_{v \rightarrow v-1}$ is the band origin wavenumber, h is Planck's constant, c the speed of light, and ν_T is the frequency of the transition, defined as the difference in energy between the upper and lower states of the transition. These energies (in cm^{-1}) are calculated with the formula:

$$E_{v, J} = \omega_e(v + 1/2) - \omega_e x_e(v + 1/2)^2 + B_v J(J + 1), \quad (54)$$

using spectroscopic values (in cm^{-1}) of $\omega_e = 1903.6$, $\omega_e x_e = 13.97$, $B_e = 1.7042$, and $\alpha_e = .0178$.¹¹ Higher-order terms in v and J are negligible. B_v is the rotational constant for vibrational level v , and is defined as

$$B_v = B_e - \alpha_e(v + 1/2). \quad (55)$$

$N_{v, J}$ in Eq. (53) is the population of the radiating vibration/rotation state and may be rewritten as

$$N_{v, J} = \frac{N_v}{Q_r} (2J + 1) \exp - (J(J + 1) B_v hc/kT) \quad (56)$$

where Q_r is the rotational partition function, k is the Boltzmann constant, and T is the temperature. N_v is the total number of molecules in vibrational state v . Given Eqs. (53) to (56) and the Einstein coefficients from Billingsley's work¹⁰ shown in Figure 16, the radiant intensity of a given transition per vibrationally excited molecule, that is, $I_{J \rightarrow J, J-1}^{v \rightarrow v-1} / N_v$, may be specified for all transitions. From this tabulation, the radiation signature of each vibrational "basis function" $\xi_v(\nu)$ is found. Integration of the intensities over a system slit function must be performed prior to fitting. In the COCHISE experiment, the luminescence is monitored by a grating spectrometer that has a triangular slit function having a constant resolution in wavelength space. Therefore, in the present analysis the convolution of the intensity predictions over the slit function is to be performed in wavelength space.

Because the transition linewidth is much narrower than the resolution, the slit function integral may be replaced by a sum, and convolution then involves only the calculation of the slit function's fractional transmission of each rotational line's intensity at line center. The nominal system resolution was taken to be $0.013 \mu\text{m}$ and the rotational temperature assumed to be 100°K , in accordance with experimental conditions. The effect of spin splitting was also included in these basis functions. Coupling of the spin and orbital angular momentum in the molecule causes the two total orbital angular momentum states to be split by 121 cm^{-1} . Similar transitions occurring within the two doublet states lie at the same frequencies (within the resolution of the experiment). However, the $\pi_{1/2}$ lies at lower energy and is preferentially thermally populated by a factor of 5.7 at 100°K . Both $\pi_{1/2}$ and $\pi_{3/2}$ spectral lines are included in the analysis.

These radiation basis functions may be related to an observed intensity at any wavelength by the relation

$$I_p(\lambda) = \sum_v N_v \xi_v(\lambda) \quad (57)$$

where the quantities N_v are proportional to the populations in level v of the excited NO molecules. Given the data $I(\lambda)$ and the functions $\xi_v(\lambda)$, defined over some wavelength interval, the quantities N_v may be determined by requiring that the square of the differences $(I_p(\lambda) - I(\lambda))$ be minimized. A computer code developed to perform this task takes the data and basis functions as input and provides the relative vibrational populations as output.

In order to provide a rapid analysis of the data, a "first pass" of basis functions was developed under the assumptions of $\Omega = 1$ and integral values of J . The best-fit computer spectra generated with these basis functions is shown in Figure 17 in comparison with the data of Figure 15. The set of curves shown at the bottom of the spectra are the individual basis functions, summed to provide the

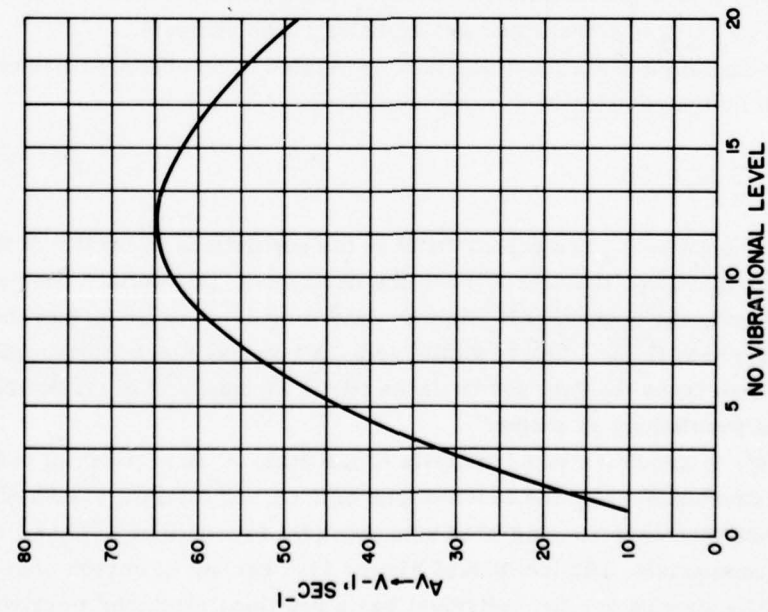


Figure 16. Predicted Einstein Coefficients for the Fundamental Band of NO as Specified in Ref. 10

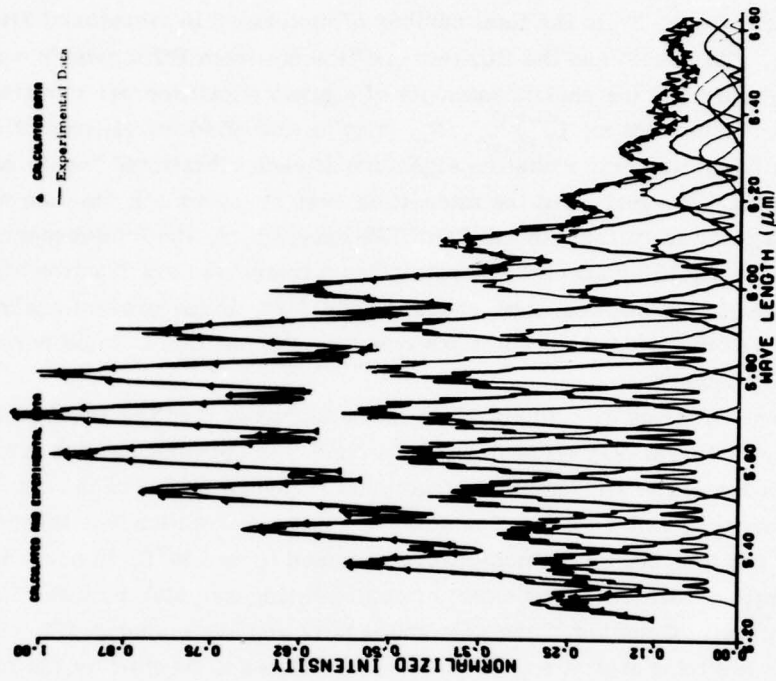


Figure 17. Comparison of Synthetic and Measured NO Fundamental Band Radiation; Approximate Basis Functions, Resolution = $0.013 \mu\text{m}$

predicted spectra. These individual basis functions represent the contribution of each vibrational level to the total intensity. As can be seen, the comparison between curve fit and data is quite good, surprisingly so considering that only approximate basis functions were used. Note that the contribution of the $v = 1 \rightarrow 0$ transition has been overestimated, because the data shows underlying spectral features in this wavelength region that are not due to NO.

More detailed basis functions were then generated and the effect of the spin states was examined. A comparison of the data with a curve fit performed using half-integral J values, but assuming all the molecules to have $\Omega = 1/2$ ($\pi_{1/2}$ state), is shown in Figure 18. The predicted Q-branches are much weaker than those observed experimentally. In addition, the synthetic spectrum seems to have greater resolution than the data. Consequently, a curve fit in which the resolution was decreased to $0.02 \mu\text{m}$ was generated and is shown in Figure 19. As can be seen, the match with the experimental data is much better in this case, and this resolution was used in all subsequent calculations. The results of a similar calculation performed assuming all the population to be in the $\pi_{3/2}$ level are presented in Figure 20. The predicted Q branches are very prominent, as expected from Eq. (52). Thus, even though the $\Omega = 1/2$ states are preferentially populated by a factor of 5.7, $\pi_{3/2}$ transitions significantly contribute to the spectrum in the Q branch regions. The fit of a synthetic spectrum, from a calculation including thermally populated $\pi_{1/2}$ and $\pi_{3/2}$ states, is compared to the experimental data in Figure 21. As can be seen, the comparison between data and curve fit is once again excellent.

A modified version of the basis function-generation program was also created for use on the PDP8 computer used for COCHISE data acquisition. Due to the PDP8's limited (16 K) active memory space, the basis functions are individually calculated, convolved, normalized, and then integerized to minimize storage volume. The least-square-fitting routine requires far too much memory space for use on the PDP8, so a new algorithm has been developed. The method involves the sequential fitting of the basis functions to the data at values near the peak intensities of the basis function P and R branches. At the 100°K temperature under which the experiment is performed, only the first 10 to 15 rotational levels of the vibration are populated. Thus, only two vibrational basis functions have significant intensity at most wavelengths. The P branch of a vibrational band occurs at almost the same wavelength as the R branch of the next higher vibration, and both bands contribute to the emitted intensity. No such overlap occurs for the R branch of the $v = 1$ transition. A fit to the emitted intensity at wavelengths near the peak of that branch permits unique determination of the population of that level. The average of 20 values calculated near the branch peak is taken as the estimate. This population is then used in determining the population of the $v = 2$ level by fitting the two

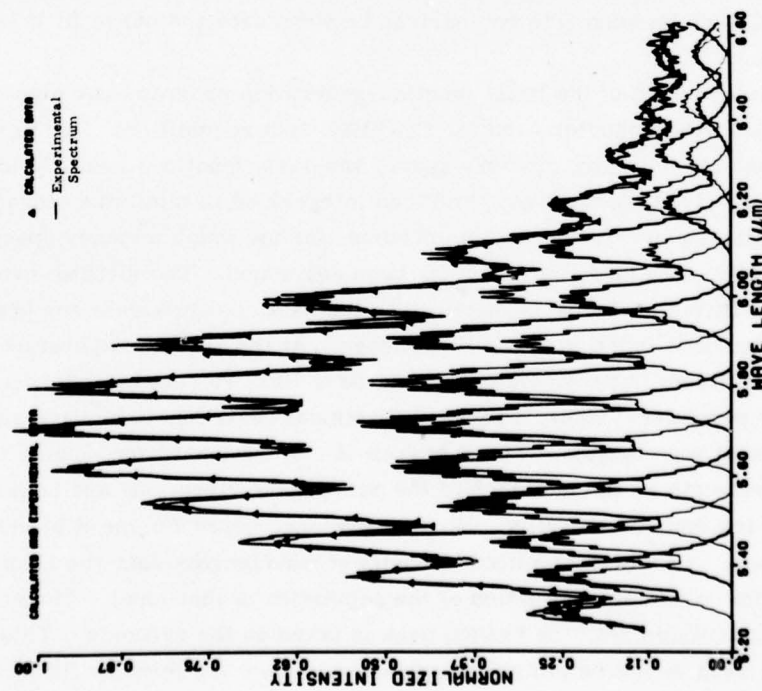


Figure 18. Comparison of Synthetic and Measured NO Fundamental Band Radiation; $\pi_{1/2}$ State Only, Resolution = 0.013 μm

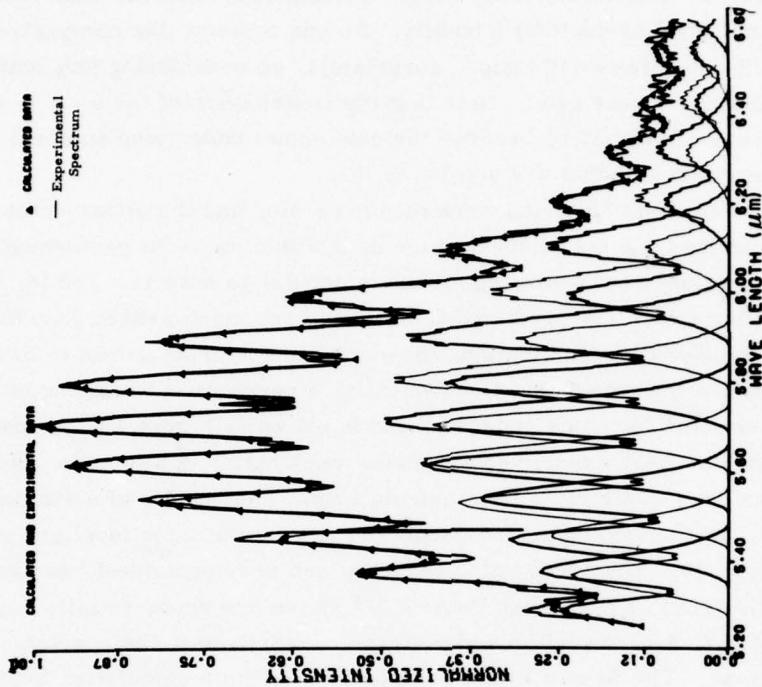


Figure 19. Comparison of Synthetic and Measured NO Fundamental Band Radiation; $\pi_{1/2}$ State Only, Resolution = 0.020 μm

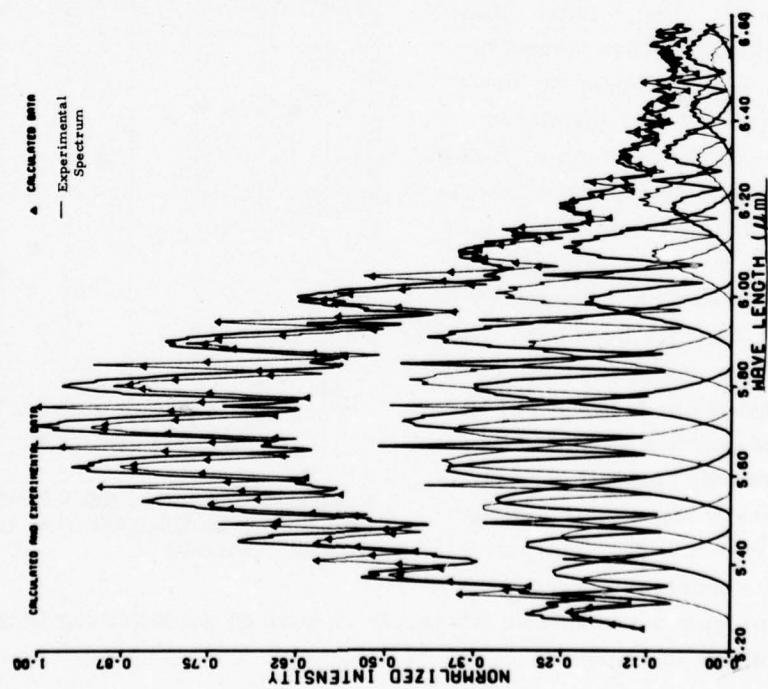


Figure 20. Comparison of Synthetic and Measured NO Fundamental Band Radiation; $\pi_{3/2}$ State Only, Resolution = 0.020 μm

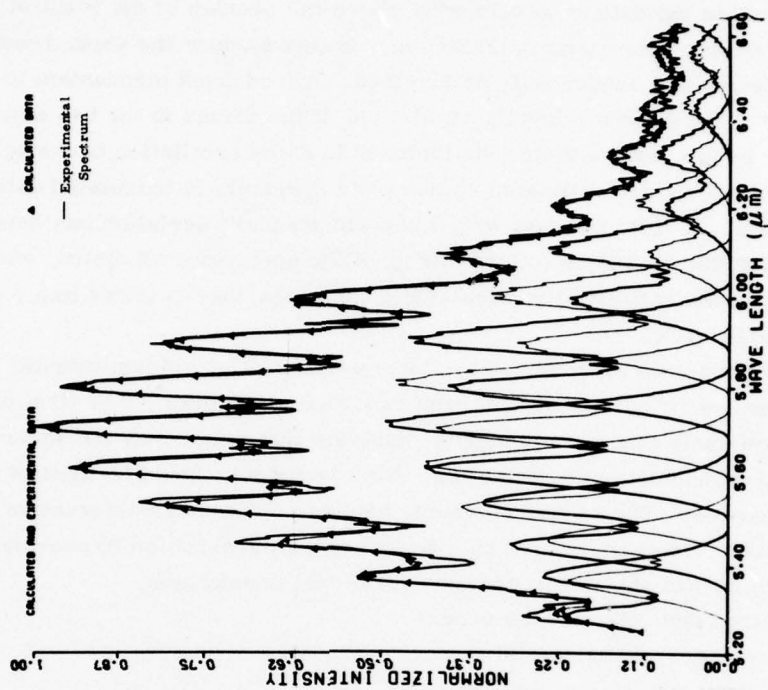


Figure 21. Final Comparison between Synthetic and Measured NO Fundamental Band Radiation; $\pi_{1/2, 3/2}$ States Assumed Thermally Populated at $T = 100^\circ\text{K}$, Resolution = 0.020 μm

basis functions to the data at wavelengths where the overlap of the P and R branches of the two vibrations is maximum. In this manner the populations of the vibrational levels are sequentially determined. A feed-back mechanism to permit modification of the previous level's population, if the values in the two adjacent levels differ by too great a factor, is included to damp oscillation of the solutions. After all populations are estimated, a complete spectrum is calculated using the basis functions. A fit to the data with 8 percent standard deviation has been achieved using this technique. Hand-fitting of the spectrum, an option, with slight modification of the sequentially calculated populations, has resulted in a 5 percent standard deviation fit.

In conclusion, two techniques have been developed for determining NO vibrational populations from fundamental band radiation signatures. The first of these is a completely self consistent computer analysis that minimizes the square of the differences between data and prediction. This technique should be used in any final data analysis. The second technique involves a computer-interactive hand-fitting technique that can be used on site during data acquisition to provide a relatively accurate estimate of the relevant vibrational populations.

The desired end result of the experiment is to relate the deduced vibrational populations to the rate constants for reaction (44). The relative vibrational populations, as determined from the data fit shown in Figure 21, are shown in Figure 22. As mentioned earlier, the population of the $v = 1$ state has been overestimated, since the data exhibits an additional radiation source in the wavelength region of the $v = 1 \rightarrow 0$ transition. Note, with the exception of level 1, that the vibrational population varies smoothly, decreasing monotonically with increasing vibrational level. (The deduced populations for levels $v = 12-13$ are only approximate, given the large background radiation in that wavelength region.) It is interesting to note that the relative vibrational populations deduced from the fits shown in Figures 17 to 20 do not differ significantly from those shown in Figure 22.

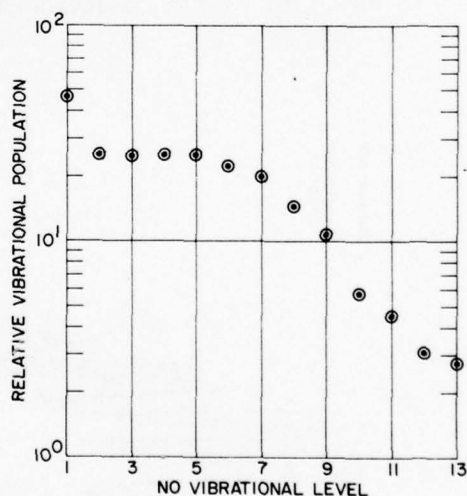


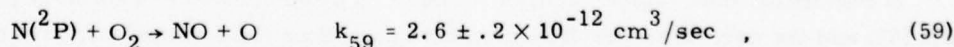
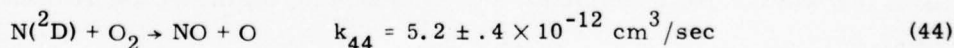
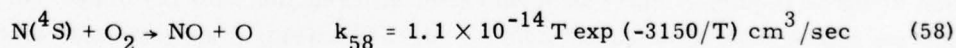
Figure 22. Relative NO Vibrational Populations as Deduced from the Data of Figure 15

A kinetic analysis is required in order to relate these vibrational populations to the rate constants for reaction (44). The first step in this analysis is to estimate the relative concentrations of the various species in the test chamber. In a microwave discharge the nitrogen atom concentration will typically be 1 percent of that of N_2 , and the $N(^2D)$, $N(^2P)$ concentrations would be 1 percent of the nitrogen atom concentration. Thus, given the total pressure of 4 mtorr, one can estimate the species concentrations; these are listed in Table 2. The large helium concentration shown in Table 2 is the result of a helium leak in the system, present at the time of the measurement. The residence time within the test chamber is estimated to be 1 msec (this estimate could be a lower bound because of the helium leak); thus, chemical reactions that occur on a time scale of <10 msec will be of interest.

Table 2. COCHISE Species Concentrations,
P = 4 mtorr, T = 100°K

Species	Concentration, Part /cm ³
O ₂	4×10^{13}
Ar	4×10^{13}
N ₂	3×10^{12}
N(⁴ S)	3×10^{10}
N(² D, ² P)	3×10^8
He	4×10^{14}

The three reactions that can produce NO in the system are:

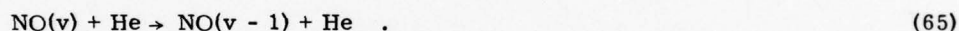
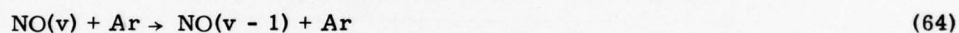
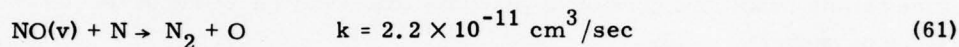


where the rate constant for reaction (58) was taken from Garvin and Hampson,¹² and those for reactions (44) and (59) are room temperatures measurements reported

12. Garvin, D., and Hampson, R. F., eds. (1974) Chemical Kinetics Data Survey VII. Tables of Rate and Photochemical Data for Modeling of the Stratosphere (Revised), NBSIR74-430, January.

by Husain et al.¹³ Reactions (44) and (59) are also the only important loss mechanisms for $N(^2D, ^2P)$. Reaction (58) may be neglected at the temperatures of interest, given its high activation energy. On the other hand, both reactions (44) and (59) may have contributed to the observed NO spectra.

The peak concentrations of NO and O that could build up within the gas residence time are estimated to be $6 \times 10^7/\text{cm}^3$; thus, any reactions between NO(v) and NO or O will be unimportant. The remaining reactions that can deactivate vibrationally excited NO are:



The Einstein coefficients for NO(v) are shown in Figure 16, and it can be seen that radiative decay will be unimportant since $(A_{v \rightarrow v-1})^{-1} > 15$ msec for all vibrational levels. Furthermore, the characteristic time for reaction (61) is approximately 1 sec, thus this reaction may be neglected. The vibration to translation (or vibration to vibration) reactions (62) to (65) are more difficult to assess inasmuch as the rate constants for these processes increase with vibrational level and are for the most part not well defined, particularly for $T = 100^\circ\text{K}$. Shown in Table 3 is the available rate constant information for these processes as well as the rate constant that would be required to provide a characteristic reaction time of 10 msec for the species concentrations listed in Table 2. As can be seen, it appears that reactions (62) to (65) will not cause vibrational deactivation of NO during the gas residence time.

In conclusion then, vibrationally excited NO will be created by reactions (44) and (59) and the only important loss mechanisms will be fluid dynamical. Therefore, the relative NO vibrational populations shown in Figure 22 are directly proportional to the NO(v) creation rates. The relative contributions of $N(^2D)$ and

13. Husain, D., Miera, S.K., and Young, A.N. (1974) J. Chem. Soc. Far. Trans. II 70:1721.

Table 3. Rate Constant Data for Vibrational Deactivation of NO

Process	Necessary Rate Constant $k(\tau = 10 \text{ msec})$ cm^3/sec	Reported Rate Constant $k \text{ cm}^3/\text{sec},$ $T = 300^\circ\text{K}$	Ref.
NO(v) + He	2.5×10^{-13}	$v = 1 \quad 1.2 \times 10^{-16}$ $v = 15 \quad 3.4 \times 10^{-14}$	14 Estimated
NO(v) + Ar	2.5×10^{-12}	<He	15
NO(v) + O ₂	2.5×10^{-12}	$v = 1 \quad 2.4 \times 10^{-14}$	16
		$v = 7 < 1.4 \times 10^{-13}$	17
NO(v) + N ₂	3.3×10^{-11}	$v = 1 \quad 1.5 \times 10^{-16}$	14
		$v = 1 \quad 1.7 \times 10^{-16}$	16

N(²P) to these creation rates cannot be ascertained until such time as the N(²D, ²P) absorption diagnostic is implemented.

Some effort has also been directed towards determining the source of the underlying radiation observed in Figure 15 in the wavelength region of 5.03 to 5.23 μm . This radiation exhibits a band-like structure and, although not shown, this structure extends down to $\approx 4.5 \mu\text{m}$ where an apparent bandhead is observed (the data are quite noisy in this region and this interpretation is open to question). The N₂O(ν_3) bandhead is at 4.5 μm , thus it is possible that the observed radiation could be due to highly vibrationally excited N₂O, that is, N₂O(00n). This suggestion remains to be confirmed by additional measurements; however, N₂O is one of the few molecules that can be formed in mixtures of active nitrogen and oxygen.

The N₂O formation mechanism remains to be identified. The accepted neutral species reaction mechanism for formation of N₂O in active N₂/O₂ mixtures involves a sequence of binary and tertiary reactions and cannot be operative at the densities and time scales of the COCHISE experiment. One possible N₂O formation mechanism appropriate to the conditions at the COCHISE facility involves the metastable

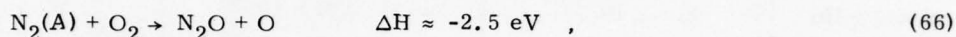
14. Stephenson, J.C. (1973) J. Chem. Phys. 59:1523.

15. Wray, K.L. (1962) J. Chem. Phys. 36:2597.

16. Murphy, R.E., Lee, E.T.P., and Hart, A.M. (1975) J. Chem. Phys. 63: 2919.

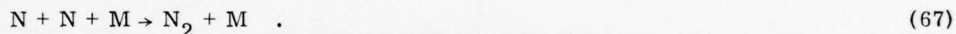
17. Whitson, M.E. Jr., Darnton, L.A., and McNeal, R.J. (1976) Chem. Phys. Lett. 41:552.

$N_2(A \ ^3\Sigma)$ state. The $N_2(A)$ state is formed in significant quantities in active nitrogen and has been found to be rapidly quenched by oxygen molecules with a room temperature rate constant of $6 \times 10^{-12} \text{ cm}^3/\text{sec}$ ¹⁸. Furthermore, it has been found^{18, 19} that oxygen atoms are formed in this quenching reaction. One possible branch for this reaction would be



which is sufficiently exothermic to allow the product N_2O to be created in high vibrational states. Reaction (66), or its equivalent, will provide the dominant chemical loss mechanism for $N_2(A)$ and would have a time constant of $4 \times 10^{-3} \text{ sec}$ in the test chamber.

The dominant formation mechanism for $N_2(A)$ state is through the nitrogen atom recombination reaction



It is estimated²⁰ that approximately one half the nitrogen molecules created by reaction (67) are formed in the A state. Since this is a three-body reaction, $N_2(A)$ state will not be produced in significant quantities in the test chamber. It will, however, be formed in the microwave discharge, and its concentration in the inlet pipe will be controlled by the formation mechanism (67) and quenching by the reaction



which has a room temperature rate constant of $5 \times 10^{-11} \text{ cm}^3/\text{sec}$.⁸ Therefore, in steady state, the $N_2(A)$ concentration may be crudely estimated to be defined by

$$N_2(A) = 0.5 k_{67} (N) (M) / k_{68} \quad (69)$$

where (N) and (M) are the nitrogen atom and total particle concentrations, respectively. The estimated inlet tube pressure is 1 to 2 torr; thus, for $k_{67} = 4.4 \times 10^{-33} \text{ cm}^6/\text{sec}^{12}$,

18. Meyer, J.A., Klosterboer, D., and Setser, D.W. (1971) J. Chem. Phys. 55:2084.

19. Meyer, J.A., Setser, D.W., and Stedman, D.H. (1970) J. Phys. Chem. 74:2238.

20. Thrush, B.A., and Wild, A.H. (1972) J. Chem. Soc. Far. Trans. I 68:2023.

$$N_2(A) \approx 3 \times 10^{-6} N(^4S) \quad . \quad (70)$$

Since this ratio would be maintained in the expansion from the inlet tube to the center of the test chamber, the estimated $N_2(A)$ concentration in the chamber would be $\approx 10^5$ part/cm³. Therefore, over the gas residence time of 1 msec, 2.4×10^4 part/cm³ of N_2O could be produced by reaction (66). This is to be compared to the concentration of NO produced by reactions (44) and (59), which has been shown to be 6×10^7 /cm³. While the estimated N_2O concentration is more than 3 orders of magnitude below that for NO, it is to be noted that $N_2O(v_3)$ radiates 25 times more strongly than NO, whereas the unidentified band radiation is less than one tenth that of the NO radiation.

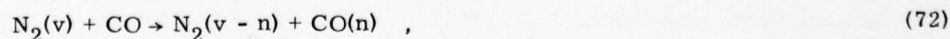
The crude order of magnitude arguments presented here indicate that it is possible that N_2O , produced by reaction (66), could be the cause of the underlying band radiation seen in Figure 15. This conjecture must be tested by more detailed measurements with more definitive data analysis. Note that reaction (66) is of considerable interest in its own right inasmuch as it would provide an upper atmospheric, or auroral, source for N_2O production.

Two other preliminary measurements have been performed on the COCHISE facility and these will be discussed briefly. In the first of these measurements, discharge excited N_2 /Ar was mixed in the chamber with a gas mixture composed of 10 percent CO/90 percent O_2 . Since the discharge excited nitrogen will be highly vibrationally excited, it was anticipated that the reaction

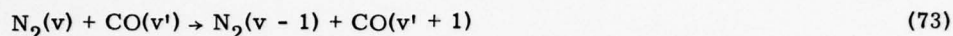


would occur and the resulting CO fluorescence could be used to provide an internal wavelength calibration for the system. The observed fluorescence in this case is shown in Figure 23. The peak to the left of the figure corresponds to the $v = 1 \rightarrow 0$ transition of CO, whose band center is at $4.666 \mu m$. Thus it was found that the nominal wavelength calibration, shown in Figure 23, was off by $0.033 \mu m$. This correction was used in NO data analysis.

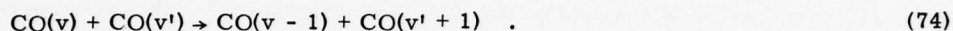
More interestingly, it can be noted that CO radiation from the transitions $v = 2 \rightarrow 1$ to $v = 5 \rightarrow 4$ was also observed. These states could have been excited by multi-quantum vibrational transfer, that is,



or alternately by a sequence of single quantum exchange reactions such as



and



Given the low density and short residence time within the test chamber, it is anticipated that reaction sequences involving multiple collisions between species produced only in the test chamber are unlikely, and that the observed fluorescence is more probably due to multi-quantum vibrational transfer. Thus it is expected that additional measurements of this type, taken under more carefully controlled conditions, will provide estimates of the relative probabilities of single and multiple quantum transfer collisions in CO.

The last measurement to be discussed was again made for calibration purposes. In this case discharge-excited N_2/Ar was mixed with Ar in the test chamber in order to determine background radiation levels in the absence of O_2 . The rather surprising spectrum observed in this case is shown in Figure 24. After a review of possible radiation sources, it was determined that this spectrum is due to fluorescence from the fundamental vibration-rotation band of CN and exhibits radiation from vibration levels as high as $v = 12$. Thus, a carbon-containing species must have been present as an impurity in the gas mix. Furthermore, this impurity must react with active nitrogen in such a manner as to directly produce highly vibrationally excited CN. Although this impurity cannot be uniquely identified at present, there is a possibility that it was CO inasmuch as CO had been one of the test gases in the run performed prior to this. No CO vibro-luminescence was seen, however, and it is possible that the CN was produced from another species, for example carbonaceous impurities in the microwave discharge. The CN precursor can be determined in future measurements.

CN formation has been previously observed²¹⁻²⁴ in mixtures of active nitrogen and CO. In these cases, however, the CN "red" ($A^2\pi \rightarrow X^2\Sigma$) and "violet" ($B^2\Sigma \rightarrow X^2\Sigma$) systems were monitored rather than the infrared emission. The production of CN in mixtures of active nitrogen/CO is of fundamental interest to areas such as laser physics,²³ and several conflicting mechanisms have been

21. Broida, H. P., and Heath, D. F. (1957) J. Chem. Phys. 26:1352.

22. Stair, A. T. Jr., Kennealy, J. P., and Murphy, R. E. (1967) J. Chem. Phys. 46:1:52.

23. Taieb, G., and Legay, F. (1970) Can. J. Phys. 48:1956.

24. Young, R. A., and Morrow, W. (1974) J. Chem. Phys. 60:1005.

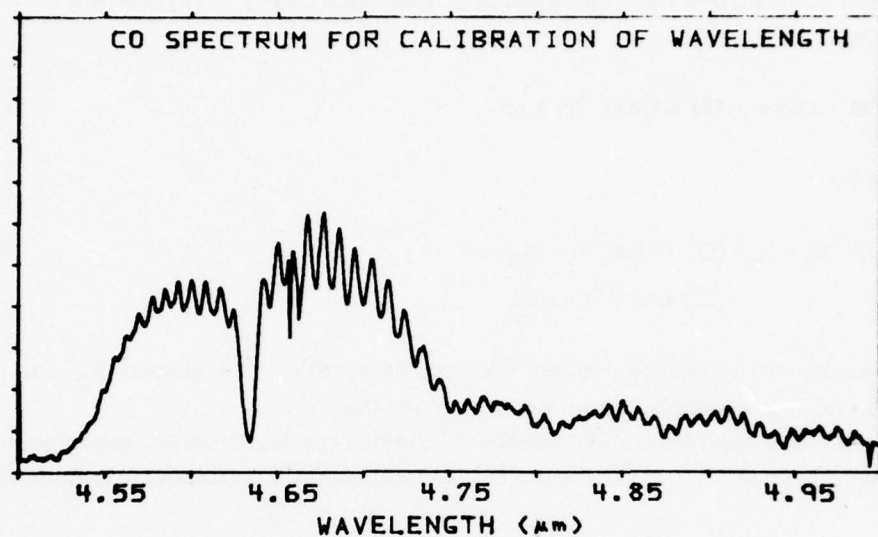


Figure 23. Observed Fluorescence for a Mix of Active Nitrogen and CO/O₂.
P = 4 mtorr, T = 100°K. Wavelength scale should be corrected by $\Delta\lambda = +0.033 \mu\text{m}$

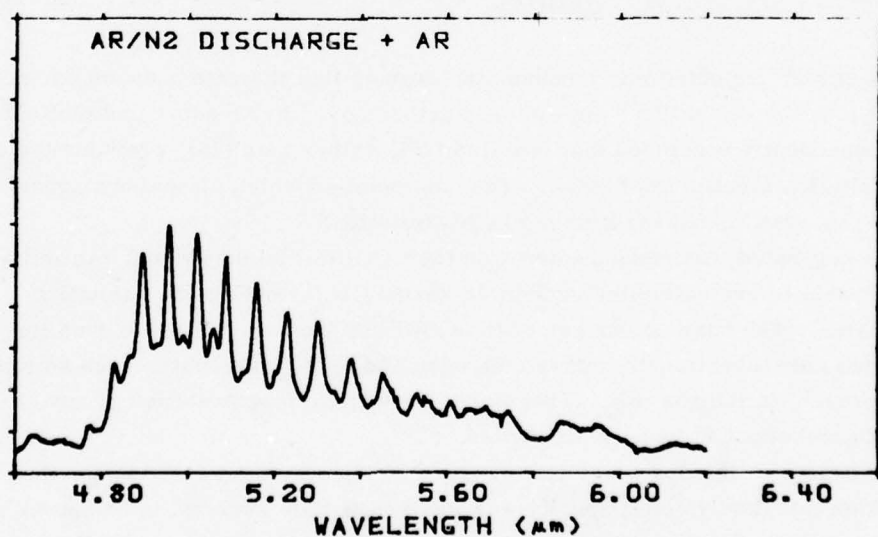


Figure 24. Observed Fluorescence From a Mix of Active Nitrogen and Argon.
P = 4 mtorr, T = 100°K. Wavelength scale should be corrected by $\Delta\lambda = +0.033 \mu\text{m}$

proposed for its formation. For example, Taieb and Legay²³ suggest the mechanism

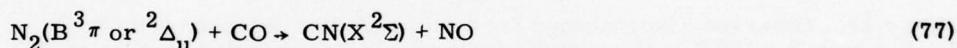


followed by

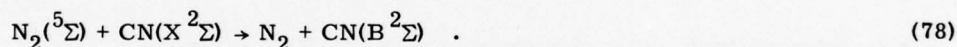


to be operative in discharge excited mixtures of N_2/CO . The quantity N_2^\dagger in reaction (76) represents highly vibrationally excited N_2 .

On the other hand Young and Morrow²⁴ studied CN formation in mixtures of active nitrogen and CO and concluded that the relevant CN formation mechanism was



followed by



Washida et al.²⁵ rejected this mechanism, arguing that the rate constant for reaction (77) must be $\ll 3 \times 10^{-19} \text{ cm}^3/\text{sec}$. Furthermore, Provencher and McKenney²⁶ have independently concluded that reaction (76), rather than (78), provides the dominant excitation mechanism for CN. The only point on which all authors agree²⁴⁻²⁶ is that $\text{N}_2(\text{A})$ state is not the source of CN excitation.

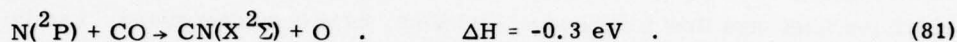
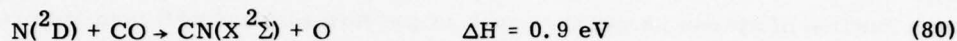
It is suggested that measurements on the COCHISE facility would be particularly valuable in evaluating the various proposed CN formation and excitation mechanisms. The basic advantage of the COCHISE facility is that the densities are so low that only vibrationally excited nitrogen and metastable states such as $\text{N}_2(\text{A})$ will be present in the gas mix. Therefore, the kinetic interpretation of any observed fluorescence is greatly simplified.

For example, the observations of Figure 23 have been analyzed under the assumption that the system impurity was indeed CO (this remains to be shown experimentally). The reactive species present in the test chamber are limited to

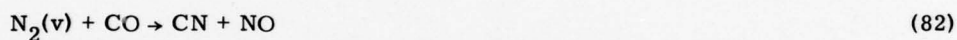
25. Washida, N., Kley, D., Becker, K. H., and Groth, W. (1975) J. Chem. Phys. 63:4230.

26. Provencher, G. M., and McKenney, D. J. (1972) Can. J. Chem. 50:2527.

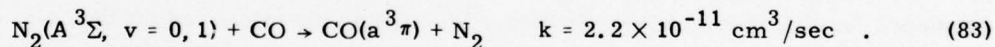
$N(^4S)$, $N(^2D)$, $N(^2P)$, $N_2(A)$, and $N_2(v)$. The possible reactions between nitrogen atoms and CO are:



The first two of these may be discarded inasmuch as they are endothermic. Although reaction (81) is exothermic, it has been shown¹³ that there is no adiabatic reaction path to the specified reactants. (The quenching of $N(^2P)$ by CO has, however, been found to be rapid,¹³ and it is possible that the reaction could proceed by a non-adiabatic transition. In any event, the exothermicity of reaction (81) is insufficient to provide the CN vibrational excitation observed.) The reaction

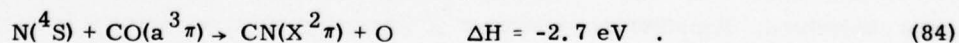


requires 5.5 eV in vibrational energy to be exothermic and may be neglected. Lastly, the reaction between $N_2(A)$ state and CO has been found¹⁸ to produce $CO(a^3\pi)$, that is,



Reaction (83) is almost thermoneutral and, thus, at room temperature the product $CO(a^3\pi)$ state may be rapidly quenched by N_2 , again reforming $N_2(A)$. This path would become much less probable at the COCHISE temperature of 100°K.

It is concluded then that the only species produced in reaction between the discharge species and CO is $CO(a^3\pi)$. A possible subsequent path for formation of CN would then be



It is interesting to note that this reaction is sufficiently exothermic to produce CN vibrationally excited to $v \approx 12$, as can be observed in the data of Figure 24. This result may well be a coincidence, but, given the present analysis as well as the controversy in the literature, it would be of value to attempt to duplicate the observations of Figure 24 under controlled conditions.

4. SUMMARY AND CONCLUSIONS

In summary, a model has been developed to describe the fluid dynamical fields within the COCHISE facility. This model has been exercised to predict expected test chamber conditions, such as pressure, temperature, and gas residence time, as a function of system parameters such as gas flow rate and wall temperature. Furthermore, limiting system operating conditions, such as the gas flow rate at which the inlet pipe flow will become turbulent, have been designated. Lastly, the computational procedure required for a more detailed flow analysis of the system has been outlined in Appendix A.

Analyses and interpretation of preliminary infrared fluorescence measurements taken on the system have also been presented. The most prominent of these was the analysis of NO fundamental vibration band radiation resulting from the chemi-excitation reaction



Two computer codes were developed that allow determination of the NO vibrational populations corresponding to the observed spectrum. The first of these provides a best least-squares-fit between the data and a computer generated spectrum. The second, developed for use on the COCHISE facility PDP8 computer, allows use of a less accurate, computer interactive, spectrum-fitting procedure. (Although developed for NO, these codes may be used for fitting the measured fundamental vibrational band spectrum of any diatomic molecule.) The NO vibrational populations corresponding to the observed spectrum were determined from the first of these codes, and it was demonstrated that these relative vibrational populations were directly proportional to the creation rates for NO(v).

Several other pieces of preliminary data were analyzed in terms of CO vibro-excitation and in terms of unique formation mechanisms for N_2O and CN. This data analysis was complicated both by a lack of diagnostic information and by insufficient low temperature kinetic data and, for the most part, must be considered as pure conjecture. Nonetheless, a number of intriguing spectral features have been observed in this preliminary data. It is suggested that the examination of such data, taken under controlled conditions, could provide a wealth of useful kinetic information.

References

1. Albini, F.A. (1965) AIAA Journal 3:1535.
2. Hubbard, E.W. (1966) AIAA Journal 4:1877.
3. Boynton, F.P. (1967) AIAA Journal 5:1703.
4. Ashkenas, H., and Sherman, F.S. (1966) The structure and utilization of supersonic free jets in low density wind tunnels, in Rarefied Gas Dynamics, Fourth Symposium, Vol. II. Academic Press, New York, pp. 84-105.
5. Bier, K., and Schmidt, B. (1961) Zeitschrift Agnew Physik 13:495.
6. Dawson, J.P. (1966) J. Spacecraft 3:218.
7. Schlichting, H. (1955) Boundary Layer Theory, McGraw Hill.
8. Lin, C.L., and Kaufman, F. (1971) J. Chem. Phys. 55:3760.
9. Mitchell, A.C.G., and Zemansky, M.W. (1934) Resonance Radiation and Excited Atoms, Cambridge, London, p 323.
10. Billingsley, F.P. (1976) J. Molecular Spectroscopy 61:53.
11. Herzberg, G. (1951) Molecular Spectra and Molecular Structure I, Spectra of Diatomic Molecules, 2nd ed., D. Van Nostrand Co., New York.
12. Garvin, D., and Hampson, R.F., eds. (1974) Chemical Kinetics Data Survey VII. Tables of Rate and Photochemical Data for Modeling of the Stratosphere (Revised), NBSIR74-430, January.
13. Husain, D., Miera, S.K., and Young, A.N. (1974) J. Chem. Soc. Far. Trans. II 70:1721.
14. Stephenson, J.C. (1973) J. Chem. Phys. 59:1523.
15. Wray, K.L. (1962) J. Chem. Phys. 36:2597.
16. Murphy, R.E., Lee, E.T.P., and Hart, A.M. (1975) J. Chem. Phys. 63: 2919.
17. Whitson, M.E. Jr., Darnton, L.A., and McNeal, R.J. (1976) Chem. Phys. Lett. 41:552.

18. Meyer, J.A., Klosterboer, D., and Setser, D.W. (1971) J. Chem. Phys. 55:2084.
19. Meyer, J.A., Setser, D.W., and Stedman, D.H. (1970) J. Phys. Chem. 74:2238.
20. Thrush, B.A., and Wild, A.H. (1972) J. Chem. Soc. Far. Trans. I 68:2023.
21. Broida, H.P., and Heath, D.F. (1957) J. Chem. Phys. 26:1352.
22. Stair, A.T. Jr., Kennealy, J.P., and Murphy, R.E. (1967) J. Chem. Phys. 1:52.
23. Taieb, G., and Legay, F. (1970) Can. J. Phys. 48:1956.
24. Young, R.A., and Morrow, W. (1974) J. Chem. Phys. 60:1005.
25. Washida, N., Kley, D., Becker, K.H., and Groth, W. (1975) J. Chem. Phys. 63:4230.
26. Provencher, G.M., and McKenney, D.J. (1972) Can. J. Chem. 50:2527.

Appendix A

Radial Flow Model for COCHISE

The analysis of Section 2 was conducted in order to make predictions of the tank centerline pressure as a function of wall temperature, mass flow/inlet tube, and inlet temperature. In the process of conducting the analysis, it was assumed that region four was a stationary gas. This approximation was made in order that the model be compatible with the manner in which the capture coefficients were measured. A more detailed model for region four was originally initiated. The model included a spatially variable mean gas velocity, gas temperature, and gas pressure. When it was realized that the capture coefficients were not known accurately enough to justify such a model, the effort was dropped. The model is documented in this appendix for two reasons: first, inaccuracies in the present model may force us to look more closely at the pressure and temperature variations in the tank and, secondly, the possibility of gas diffusing from the chamber wall to the tank centerline could be assessed more accurately using the radial flow model that we will now describe.

In Section 2.6, we determined that most of the flow is in the plane perpendicular to the tank axis. Figure 12 of the main text illustrates that the flow approaches the wall as though it were coming from a line source on the tank centerline. Hence, we define a radial flow model with axial symmetry. The mass originates at a line source on the axis of the tank and flows radially toward the sink at the cryogenically cooled walls.

Let us define the reference temperature, pressure, density, and velocity as

$$T_{\text{ref}} = T_i \quad (\text{A-1})$$

$$p_{\text{ref}} = \dot{M} u_{\text{ref}} / 2\pi R Y \quad (\text{A-2})$$

$$\rho_{\text{ref}} = p_{\text{ref}} / \mathcal{R} T_i \quad (\text{A-3})$$

and

$$u_{\text{ref}} = \sqrt{2\mathcal{R} T_i} \quad (\text{A-4})$$

where \mathcal{R} is the gas constant and R is the radius of the tank.

The dimensionless variables are defined as

$$\theta = T/T_i \quad (\text{A-5})$$

$$v = u/u_{\text{ref}} \quad (\text{A-6})$$

$$\omega = p/p_{\text{ref}} \quad (\text{A-7})$$

$$\phi = \rho/\rho_{\text{ref}} \quad (\text{A-8})$$

and

$$\alpha = r/R \quad (\text{A-9})$$

The Reynolds and Knudsen numbers become

$$Re = \dot{M} / \mu \pi Y = O(10) \quad (\text{A-10})$$

and

$$Kn \approx v/R_e \approx O\left(\frac{1}{10}\right) \quad (\text{A-11})$$

respectively. The approximate values of Re and Kn suggests that an appropriate description of the tank flow can be made with the use of the Navier Stokes equations and "slip flow" boundary conditions.¹

1. Schaaf, S.A. (1958) Flow of rarefied gases, in Fundamentals of Gas Dynamics, ed. H.W. Emmons, Princeton Univ. Press, 1958, pp. 709-719.

Navier Stokes Equations

The equation of continuity for radial flow with axial symmetry is expressed as

$$\alpha \phi v = 1 \quad . \quad (A-12)$$

The momentum equations is expressed

$$\phi v \frac{\partial v}{\partial \alpha} + \frac{1}{2} \frac{\partial \omega}{\partial \alpha} = \frac{1}{\text{Re}} \left(\frac{\partial^2 v}{\partial \alpha^2} + \frac{1}{\alpha} \frac{\partial v}{\partial \alpha} - \frac{v}{\alpha^2} \right) \quad (A-13)$$

where we have assumed that the viscosity is constant. The energy equation becomes

$$\phi v \frac{\partial \theta}{\partial \alpha} = \left(\frac{\gamma - 1}{\gamma} \right) v \frac{\partial \omega}{\partial \alpha} + \frac{1}{\text{Pr Re}} \left(\frac{\partial^2 \theta}{\partial \alpha^2} + \frac{1}{\alpha} \frac{\partial \theta}{\partial \alpha} \right) + \frac{4(\gamma - 1)}{\gamma \text{Re}} \left[\left(\frac{\partial v}{\partial \alpha} \right)^2 + \frac{v^2}{\alpha^2} \right] \quad , \quad (A-14)$$

where the second and third terms on the right are the conduction and dissipation, respectively, and Pr is the Prandtl number. The equation of state is expressed as

$$\omega = \phi \theta \quad . \quad (A-15)$$

The density ϕ and the pressure ω may be eliminated via the continuity and state equations, respectively. Second-order equations for the velocity v and temperature θ result:

$$\frac{\partial^2 v}{\partial \alpha^2} = \frac{v}{\alpha^2} - \frac{1}{\alpha} \frac{\partial v}{\partial \alpha} + \text{Re} \left[\frac{1}{\alpha} \frac{\partial v}{\partial \alpha} - \frac{\theta}{2\alpha^2 v^2} \left(\alpha \frac{\partial v}{\partial \alpha} + v \right) + \frac{1}{2\alpha v} \frac{\partial \theta}{\partial \alpha} \right] \quad (A-16)$$

and

$$\begin{aligned} \frac{\partial^2 \theta}{\partial \alpha^2} = & - \frac{1}{\alpha} \frac{\partial \theta}{\partial \alpha} - \frac{4 \text{Pr} (\gamma - 1)}{\gamma} \left[\left(\frac{\partial v}{\partial \alpha} \right)^2 + \frac{v^2}{\alpha^2} \right] + \text{Pr Re} \frac{1}{\alpha} \frac{\partial \theta}{\partial \alpha} \\ & - \text{Pr Re} \left(\frac{\gamma - 1}{\gamma} \right) \left[\frac{1}{\alpha} \frac{\partial \theta}{\partial \alpha} - \frac{\theta}{\alpha} \left(\frac{1}{v} \frac{\partial v}{\partial \alpha} + \frac{1}{\alpha} \right) \right] \quad . \end{aligned} \quad (A-17)$$

Wall Boundary Conditions

Let us assume that the gas at the wall has a Maxwellian velocity distribution characteristic of the gas temperature T_w , pressure p_w , mean velocity u_w , and density ρ_w :

$$f^M = \frac{\rho_w}{(2\pi \mathcal{R} T_w)^{3/2}} \exp \left[-\frac{(\xi_1 - u_w)^2 + \xi_2^2 + \xi_3^2}{2\mathcal{R} T_w} \right], \quad (A-18)$$

where ξ_1 is the molecular velocity normal to the wall and ξ_2 and ξ_3 are tangent to the walls. Let us also assume that all molecules leaving the wall are thermally accommodated to the wall temperature τ_w and obey a wall Maxwellian distribution function characteristic of that temperature:

$$f_w = N \exp \left[-\frac{\xi_1^2 + \xi_2^2 + \xi_3^2}{2\mathcal{R} \tau_w} \right], \quad (A-19)$$

where N is to be determined.

The flux of mass per unit area toward the wall (M^+) is determined in a manner described by Schaaf¹:

$$M^+ = \int_{-\infty}^{\infty} \int_{-\infty}^{\infty} \int_0^{\infty} \xi_1 f^M d\xi_1 d\xi_2 d\xi_3 \quad (A-20)$$

or

$$M^+ = \frac{p_w F_1}{(2\pi \mathcal{R} T_w)^{1/2}}, \quad (A-21)$$

where

$$F_1 = \exp(-\beta^2) + \sqrt{\pi} \beta + \sqrt{\pi} \beta \operatorname{erf} \beta, \quad (A-22)$$

β is the speed ratio,

$$\beta = u_w / (2\mathcal{R} T_w)^{1/2}, \quad (A-23)$$

and

$$\operatorname{erf} \beta = \frac{2}{\sqrt{\pi}} \int_0^{\beta} e^{-x^2} dx . \quad (\text{A-24})$$

In a similar manner, we obtain the flux of translational energy toward the wall:

$$E_{\text{tr}}^+ = \int_{-\infty}^{\infty} \int_{-\infty}^{\infty} \int_0^{\infty} \xi_1 (\xi_1^2/2) f^M d\xi_1 d\xi_2 d\xi_3 \quad (\text{A-25})$$

or

$$E_{\text{tr}}^+ = p_w (2\mathcal{R} T_w)^{1/2} F_2 / \sqrt{\pi} , \quad (\text{A-26})$$

where

$$F_2 = (1 + \beta^2/2) \exp(-\beta^2) + (\beta^2 + 5/2) \beta (1 + \operatorname{erf} \beta) \sqrt{\pi}/2 . \quad (\text{A-27})$$

In addition to translational energy, each molecule carries j internal modes:

$$j = (5 - 3\gamma)/(\gamma - 1) . \quad (\text{A-28})$$

Each mode possesses internal energy $\mathcal{R} T_w/2$. Hence, the flux of internal energy is

$$E_{\text{int}}^+ = j \left(\frac{\mathcal{R} T_w}{2} \right) M^+ . \quad (\text{A-29})$$

The mass flux away from the wall is denoted by M^- :

$$M^- = - \int_{-\infty}^{\infty} \int_{-\infty}^{\infty} \int_0^0 \xi_1 f_w d\xi_1 d\xi_2 d\xi_3 \quad (\text{A-30})$$

or

$$M^- = 2 \pi N (\mathcal{R} T_w)^2 . \quad (\text{A-31})$$

The translational energy flux from the wall is

$$E_{tr}^- = - \int_{-\infty}^{\infty} \int_{-\infty}^{\infty} \int_{-\infty}^0 \xi_1 (\xi^2/2) f_w d\xi_1 d\xi_2 d\xi_3 \quad (A-32)$$

or

$$E_{tr}^- = 4 \pi N (\mathcal{R} \tau_w)^3, \quad (A-33)$$

and the flux of internal modes is

$$E_{int}^- = j \left(\frac{\mathcal{R} \tau_w}{2} \right) M^-. \quad (A-34)$$

From the positive and negative mass fluxes, we define the sticking coefficient S in much the same way that the capture coefficient is defined, except that the mass flux terms now contain the mean flow u_w :

$$S = \frac{M^+ - M^-}{M^+}. \quad (A-35)$$

From the mass and energy fluxes at the wall, we express the conservation of mass and energy through the tank. Hence,

$$(M^+ - M^-) 2 \pi R Y = 2 \dot{M} \quad (A-36)$$

and

$$(E_{tr}^+ + E_{int}^+ - E_{tr}^- - E_{int}^-) 2 \pi R Y = 2 \dot{M} C_p T_i, \quad (A-37)$$

where T_i is approximately the total temperature of the inlet gas.

Equations (A-35) through (A-37) are three independent equations in N , T_w , and p_w . Their solutions yield

$$T_w/T_i = F_3 (1 - S)(\tau_w/T_i) + 2\gamma SF_3/(\gamma + 1) \quad (A-38)$$

and

$$p_w/p_{ref} = 2\sqrt{\pi} \sqrt{T_w/T_i} SF_1, \quad (A-39)$$

where

$$F_3 = (4 + j)/(4 F_2/F_1 + j) \quad (A-40)$$

The equations of state and continuity are used to relate the speed ratio to the sticking coefficient,

$$S = 2\sqrt{\pi} \beta / F_1 \quad (A-41)$$

Equations (A-38) through (A-41) express the boundary conditions to be imposed on the gas at the wall. The gas temperature T_w , pressure p_w , and velocity u_w (or speed ratio β) are expressed as functions of the wall temperature τ_w , inlet gas temperature T_i , sticking coefficient S , and the mass flow per inlet tube \dot{M} .

Before proceeding with the analysis, let us examine the wall boundary conditions in more detail. Figure A-1 illustrates the gas temperature as a function of sticking coefficient for specific values of wall temperature. For values of S near zero, the gas assumes the wall temperature. This result was built into the model when it was assumed that the molecules that don't stick to the wall are thermally accommodated. As the sticking coefficient increases, molecules are removed from the tank and not replaced with cold molecules from the wall. Hence, the gas temperature increases with sticking coefficient. This trend continues until the sticking coefficient becomes sufficiently close to unity that the wall offers no back pressure. The gas expands as though it were expanding to a vacuum, and the gas temperature decreases in a supersonic expansion. The speed ratio β approaches infinity as the sticking coefficient approaches unity. Figure A-2 illustrates the gas pressure as a function of gas temperature T_w , wall temperature τ_w , and sticking coefficient S . As $S \rightarrow 0$, the pressure increases beyond limit because we assumed a constant influx of mass \dot{M} . For increasing values of S , the pressure decreases and temperature increases until we approach $S > 0.9$, where the gas expands supersonically toward the wall with decreasing temperature and pressure.

Source Boundary Conditions

In order to integrate Eqs. (A-16) and (A-17) from the tank centerline to the wall, we must specify four boundary conditions on v and θ . We have determined v_w and θ_w and must now determine two conditions on, or near, the tank centerline. If we consider the flux of mass to be transonic at some radius α^* , then the boundary conditions become

$$v = v^* = \sqrt{\gamma/(\gamma + 1)} \quad (A-42)$$

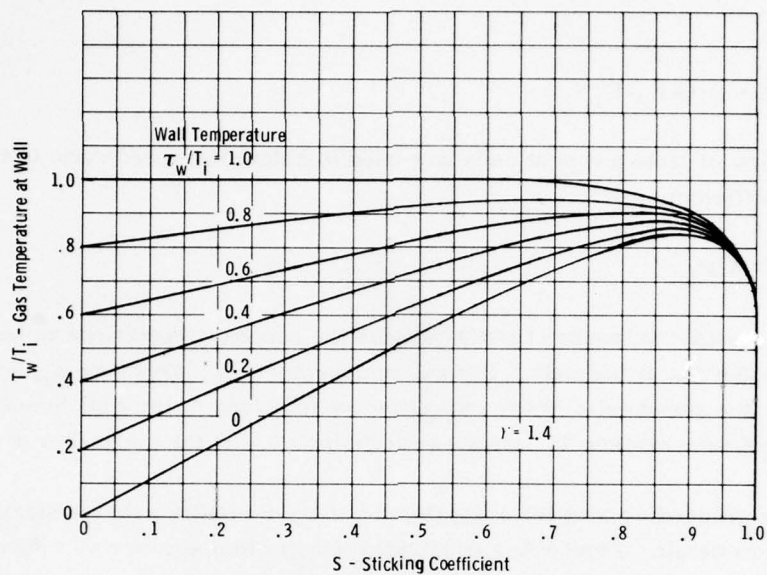


Figure A-1. Gas Temperature at Wall

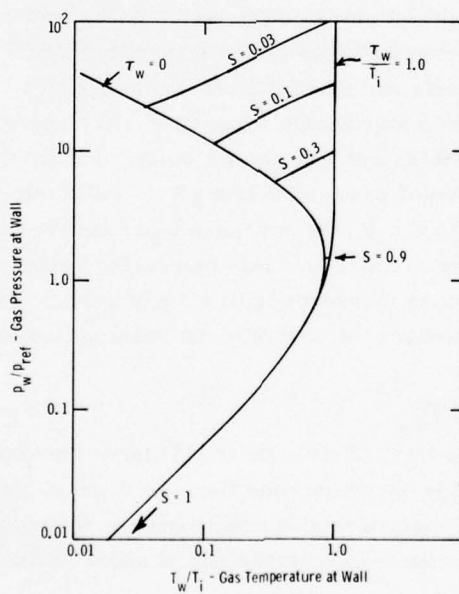


Figure A-2. Gas Pressure at Wall

and

$$\theta = \theta^* = 2/(\gamma + 1) \quad (\text{A-43})$$

at

$$\alpha = \alpha^* = \sqrt{\frac{\gamma + 1}{\gamma}} \left(\frac{\gamma + 1}{2} \right)^{1/\gamma - 1} \frac{1}{\omega_o}, \quad (\text{A-44})$$

where ω_o is the unknown value of p_{o3}/p_{ref} , the quantity that we are attempting to calculate. Mathematically, we can consider adjusting ω_o until one wall boundary condition is satisfied. Integration of the governing equations requires the specification of the gradients in θ and v at $\alpha = \alpha^*$. Since the Navier Stokes equations were introduced to describe the heat conduction at the wall, we assume that the transonic flow at the source is inviscid and the gradients are related by

$$\left. \frac{\partial \theta}{\partial \alpha} \right|_{\alpha^*} = \frac{-2(\gamma - 1)}{\gamma} v^* \left. \frac{\partial v}{\partial \alpha} \right|_{\alpha^*}. \quad (\text{A-45})$$

Since, in the inviscid limit, both gradients are infinite at the sonic point, we must choose some bounded value of $\partial v / \partial \alpha$ to start the integrations and adjust that gradient until the second wall boundary condition is satisfied.

Computational Procedure

- 1) Specify γ , Pr , \dot{M} and μ ($Re = \dot{M}/\mu\pi Y$).
- 2) Specify Arbitrary Starting Conditions.
 - i) $\omega_o = p_{o3}/p_{ref}$
 - ii) $grad^* = \partial v / \partial \alpha$ at α^* .
- 3) Determine Initial Conditions.
 - i) v^* from (A-42)
 - ii) θ^* from (A-43)
 - iii) α^* from (A-44)
 - iv) $\partial \theta / \partial \alpha$ from (A-45).
- 4) Integrate (A-16) and (A-17) from $\alpha = \alpha^*$ to $\alpha = 1$. Obtain v_w and θ_w at $\alpha = 1$.
- 5) From the definition of β , $\beta = v_w / \sqrt{\theta_w}$.
- 6) Calculate $erf \beta$, F_1 , F_2 and F_3 as defined.
- 7) Determine S from (A-41).

- 8) Determine τ_w compatible with (A-38):

$$\frac{\tau_w}{T_i} = \frac{\theta_w}{(1-S)F_3} - \frac{2\gamma S}{(\gamma+1)(1-S)} \quad .$$

- 9) Repeat for an array of values of grad.*
 10) Parametrically replace grad* with the wall temperature τ_w/T_i .
 11) Have generated, at fixed \dot{M} , γ , Pr, and μ :

$$\frac{T_w}{T_i} = \text{Fct} \left(\frac{\tau_w}{T_i}, \omega_o \right)$$

$$\frac{u_w}{u_{\text{ref}}} = \text{Fct} \left(\frac{\tau_w}{T_i}, \omega_o \right)$$

$$S = \text{Fct} \left(\frac{\tau_w}{T_i}, \omega_o \right) \quad .$$

- 12) Require data or theory for $S(\tau_w, T_w, u_w)$.
 13) Steps 11) and 12) \Rightarrow 4 relationships for S , u_w , T_w and ω_o in terms of the known values of T_i and τ_w . Hence we now have $p_{O_3}(T_i, \tau_w, M)$.

Unfortunately, step 12 is a bottleneck. Dawson's² data gives $S(T_i, \tau_w)$ and that data is insufficient for this model. More detailed models for the sticking coefficients are required before the radial flow model is justified.

References

1. Schaaf, S.A. (1958) Flow of rarefied gases, in Fundamentals of Gas Dynamics, ed. H.W. Emmons, Princeton Univ. Press, 1958, pp. 709-719.
2. Dawson, J.P. (1966) J. Spacecraft 3:218.

DNA DISTRIBUTION LIST

DIRECTOR
DEFENSE ADVANCED RSCH PROJ AGENCY
ARCHITECT BUILDING
1400 WILSON BLVD.
ARLINGTON, VA 22209
ATTN LTC W A WHITAKER

DIRECTOR
DEFENSE ADVANCED RSCH PROF AGENCY
ARCHITECT BUILDING
1400 WILSON BLVD.
ARLINGTON, VA 22209
ATTN MAJOR GREGORY CANAVAN

DEFENSE DOCUMENTATION CENTER
CAMERON STATION
ALEXANDRIA, VA 22314
ATTN TC

DEFENSE DOCUMENTATION CENTER
CAMERON STATION
ALEXANDRIA, VA 22314
ATTN TC

DIRECTOR
DEFENSE NUCLEAR AGENCY
WASHINGTON, DC 20305
ATTN RAAE CHARLES A BLANK

DIRECTOR
DEFENSE NUCLEAR AGENCY
WASHINGTON, DC 20305
ATTN TITL TECH LIBRARY

DIRECTOR
DEFENSE NUCLEAR AGENCY
WASHINGTON, DC 20305
ATTN TITL TECH LIBRARY

DIRECTOR
DEFENSE NUCLEAR AGENCY
WASHINGTON, DC 20305
ATTN TISI ARCHIVES

DIRECTOR
DEFENSE NUCLEAR AGENCY
WASHINGTON, DC 20305
ATTN RAEV HAROLD C FITZ, JR

DIRECTOR
DEFENSE NUCLEAR AGENCY
WASHINGTON, DC 20305
ATTN RAAE MAJ. J. MAYO

DIRECTOR
DEFENSE NUCLEAR AGENCY
WASHINGTON, DC 20305
ATTN RAAE G. SOPER

DIRECTOR
DEFENSE NUCLEAR AGENCY
WASHINGTON, DC 20305
ATTN MAJOR R. BIGONI

DIR OF DEFENSE RSCH & ENGR
DEPARTMENT OF DEFENSE
WASHINGTON DC 20301
ATTN DD/S&SS (OS) DANIEL BROCKWAY

DIR OF DEFENSE RSCH & ENGR
DEPARTMENT OF DEFENSE
WASHINGTON, DC 20301
ATTN DD/SS&SS DANIEL BROCKWAY

COMMANDER
FIELD COMMAND
DEFENSE NUCLEAR AGENCY
KIRTLAND AFB, NM 87115
ATTN FCPR

CHIEF LIVERMORE DIVISION
FLD COMMAND DNA
LAWRENCE LIVERMORE LAB
P.O. BOX 808
LIVERMORE, CA 94550
ATTN FCPR

COMMANDER/DIRECTOR
ATMOSPHERIC SCIENCES LABORATORY
U S ARMY ELECTRONICS COMMAND
WHITE SANDS MISSILE RANGE, NM 88002
ATTN DRSEL-BL-SY-A F. NILES

COMMANDER/DIRECTOR
ATMOSPHERIC SCIENCES LABORATORY
U S ARMY ELECTRONICS COMMAND
WHITE SANDS MISSILE RANGE, NM 88002
ATTN H. BALLARD

COMMANDER
HARRY DIAMOND LAB
2800 POWDER MILL RD
ADELPHI MD 20783
ATTN DRXDO-NP, F.H. WIMINETZ

COMMANDER
U S ARMY NUCLEAR AGENCY
FORT BLISS, TX 79916
ATTN MONA-WE

DIRECTOR
BMD ADVANCED TECH CTR
HUNTSVILLE, AL 35807
ATTN ATC-T, M CAPPS

DIRECTOR
BMD ADVANCED TECH CTR
HUNTSVILLE, AL 35807
ATTN ATC-O, W. DAVIES

DEP.CHIEF OF STAFF FOR RSCH, DEV&ACQ
DEPARTMENT OF THE ARMY
WASHINGTON DC 20310
ATTN MCB DIVISION

DEP.CHIEF OF STAFF FOR TSCH, DEV&ACQ
DEPARTMENT OF THE ARMY
WASHINGTON, DC 20310
ATTN DAMA-CSZ-C

DEP.CHIEF OF STAFF FOR RSCH, DEV&ACQ
DEPARTMENT OF THE ARMY
WASHINGTON DC 20310
ATTN DAMA-WSZC

DIRECTOR
U S ARMY BALLISTIC RESEARCH LABS
ABERDEEN PROVING GROUNDS, MD 21005
ATTN DRXRD-AM, G. KELLER

DIRECTOR
U S ARMY BALLISTIC RESEARCH LABS
ABERDEEN PROVING GROUNDS, MD 21005
ATTN DRXRD-BSP, J. HEIMERL

DIRECTOR
U S ARMY BALLISTIC RESEARCH LABS
ABERDEEN PROVING GROUNDS, MD 21005
ATTN JOHN MESTER

DIRECTOR
U S ARMY BALLISTIC RESEARCH LABS
ABERDEEN PROVING GROUNDS, MD 21005
ATTN TECH LIBRARY

COMMANDER
U S ARMY ELECTRONICS COMMAND
FOR MONMOUTH, N.J. 37703
ATTN INST FOR EXPL RESEARCH

COMMANDER
U S ARMY ELECTRONICS COMMAND
FOR MONMOUTH, N.J. 37703
ATTN DRSEL

COMMANDER
U S ARMY ELECTRONICS COMMAND
FOR MONMOUTH, N.J. 37703
ATTN STANLEY KRONENBERGER

COMMANDER
U S ARMY ELECTRONICS COMMAND
FORT MONMOUTH, N.J. 37703
ATTN WEAPONS EFFECTS SECTION

COMMANDER
US ARMY FOREIGN SCIENCE & TECH CTR
220 7TH STREET, NE
CHARLOTTESVILLE VA 29901
ATTN ROBERT JONES

CHIEF
US ARMY RESEARCH OFFICE
P.O. BOX 12211
TRIANGLE PARK, N.C. 27709
ATTN ROBERT MACE

COMMANDER
NAVAL OCEANS SYSTEMS CENTER
SAN DIEGO, CA 92152
ATTN CODE 2200 ILAN ROTHMULLER

COMMANDER
NAVAL OCEANS SYSTEMS CENTER
SAN DIEGO, CA 92152
ATTN CODE 2200 WILLIAM MOLER

COMMANDER
NAVAL OCEANS SYSTEMS CENTER
SAN DIEGO, CA 92152
ATTN CODE 2200 HERBERT HUGHES

COMMANDER
NAVAL OCEANS SYSTEMS CENTER
SAN DIEGO, CA 92152
ATTN CODE 2200 RICHARD PAPPERT

COMMANDER
NAVAL OCEANS SYSTEMS CENTER
SAN DIEGO, CA 92152
ATTN CODE 2200 JURGEN R RICHTER

DIRECTOR
NAVAL RESEARCH LABORATORY
WASHINGTON, DC 20375
ATTN CODE 7712 DOUGLAS P MCNUTT

DIRECTOR
NAVAL RESEARCH LABORATORY
WASHINGTON, DC 20375
ATTN CODE 7701 JACK D BROWN

DIRECTOR
NAVAL RESEARCH LABORATORY
WASHINGTON, DC 20375
ATTN CODE 2600 TECH LIB

DIRECTOR
NAVAL RESEARCH LABORATORY
WASHINGTON, DC 20375
ATTN CODE 7127 CHARLES Y JOHNSON

DIRECTOR
NAVAL RESEARCH LABORATORY
WASHINGTON, DC 20375
ATTN CODE 7700 TIMOTHY P COFFEY

DIRECTOR
NAVAL RESEARCH LABORATORY
WASHINGTON, DC 20375
ATTN CODE 7709 WAHAB ALI

DIRECTOR
NAVAL RESEARCH LABORATORY
WASHINGTON DC 20375
ATTN CODE 7750 DARRELL F STROBEL

DIRECTOR
NAVAL RESEARCH LABORATORY
WASHINGTON, DC 20375
ATTN CODE 7750 PAUL JULUENNE

DIRECTOR
NAVAL RESEARCH LABORATORY
WASHINGTON, DC 20375
ATTN CODE 7750 J. FEDDER

DIRECTOR
NAVAL RESEARCH LABORATORY
WASHINGTON, DC 20375
ATTN CODE 7750 S. OSSAKOW

DIRECTOR
NAVAL RESEARCH LABORATORY
WASHINGTON, DC 20375
ATTN CODE 7750 J. DAVIS

COMMANDER
NAVAL SURFACE WEAPONS CENTER
WHITE OAK, SILVER SPRING, MD 20910
ATTN CODE WA501 NAVY NUC PRGMS OFF

COMMANDER
NAVAL SURFACE WEAPONS CENTER
WHITE OAK, SILVER SPRING, MD 20910
ATTN TECHNICAL LIBRARY

SUPER INTENDENT
NAVAL POST GRADUATE SCHOOL
MONTEREY, CA 93940
ATTN TECH REPORTS LIBRARIAN

COMMANDER
NAVAL ELECTRONICS SYSTEMS COMMAND
NAVAL ELECTRONICS SYS COM HQS
ATTN PME 117

COMMANDER
NAVAL INTELLIGENCE SUPPORT CTR
4301 SUITLAND RD. BLDG 5
WASHINGTON, DC 20390
ATTN DOCUMENT CONTROL

AF GEOPHYSICS LABORATORY, AFSC
HANSCOM AFB, MA 01731
ATTN LKB KENNLTH S W CHAMPION

AF GEOPHYSICS LABORATORY, AFSC
HANSCOM AFB, MA 01731
ATTN OPR ALVA T STAIR

AF GEOPHYSICS LABORATORY, AFSC
HANSCOM AFB MA 01731
ATTN OPR-1 J. ULWICK

AF GEOPHYSICS LABORATORY AFSC
HANSCOM AFB, MA 01731
ATTN OPR-1 R. MURPHY

AF GEOPHYSICS LABORATORY, AFSC
HANSCOM AFB, MA 01731
ATTN OPR-1 J. KENNEALY

AF GEOPHYSICS LABORATORY, AFSC
HANSCOM AFB, MA 01731
ATTN PHG JC MCCLAY

AF GEOPHYSICS LABORATORY, AFSC
HANSCOM AFB, MA 01731
ATTN LKD ROCCO NARCISI

AF GEOPHYSICS LABORATORY, AFSC
HANSCOM AFB, MA 01731
ATTN LKO, R. HUFFMAN

AF WEAPONS LABORATORY, AFSC
KIRTLAND, AFB, NM 87117
ATTN MAJ. GARY GANONG, DYM

COMMANDER
ASD
WPAFB, OH 45433
ATTN ASD-YH-EX LTC ROBERT LEVERETTE

SAMSO/AW
POST OFFICE BOX 92960
WORLDWAY POSTAL CENTER
LOS ANGELES, CA 90009
ATTN SZJ MAJOR LAWRENCE DOAN

SAMSO/SW
P.O. BOX 92960
WORLDWAY POSTAL CENTER
LOS, ANGELES, CA 90009
ATTN AW

AFTAC
PATRICK AFB, FL 32925
ATTN TECH LIBRARY

AFTAC
PATRICK AFB, FL 32925
ATTN TD

HQ
AIR FORCE SYSTEMS COMMAND
ANDREWS AFB
WASHINGTON, DC 20331
ATTN DLS

HQ
AIR FORCE SYSTEMS COMMAND
ANDREWS AFB
WASHINGTON, DC 20331
ATTN TECH LIBRARY

HQ
AIR FORCE SYSTEMS COMMAND
ANDREWS AFB
WASHINGTON, DC 20331
ATTN DLCAE

HQ
AIR FORCE SYSTEMS COMMAND
ANDREWS AFB
WASHINGTON, DC 20331
ATTN DLTW

HQ
AIR FORCE SYSTEMS COMMAND
ANDREWS AFB
WASHINGTON, DC 20331
ATTN DLXP

HQ
AIR FORCE SYSTEMS COMMAND
ANDREWS AFB
WASHINGTON, DC 20331
ATTN SDR

HQ USAF/RD
WASHINGTON, DC 20330
ATTN RDQ

COMMANDER
ROME AIR DEVELOPMENT CTR
GRIFFISS AFB, NY 13440
ATTN JJ. SIMONS OC SC

DIVISION OF MILITARY APPLICATION
U S ENERGY RSCH & DEV ADMIN
WASHINGTON, DC 20545
ATTN DOC CON

LOS ALAMOS SCIENTIFIC LABORATORY
P.O. BOX 1663
LOS, ALAMOS, NM 87545
ATTN DOC CON FOR R A JEFFRIES

LOS ALAMOS SCIENTIFIC LABORATORY
P.O. BOX 1663
LOS, ALAMOS, NM 87545
ATTN DOC CON FOR CR MEHL ORG 5230

LOS ALAMOS SCIENTIFIC LABORATORY
P.O. BOX 1663
LOS, ALAMOS, NM 87545
ATTN DOC CON FOR H V ARGO

LOS ALAMOS SCIENTIFIC LABORATORY
P.O. BOX 1663
LOS, ALAMOS, NM 87545
ATTN DOC CON FOR M. TIERNEY J-10

LOS ALAMOS SCIENTIFIC LABORATORY
P.O. BOX 1663
LOS, ALAMOS, NM 87545
ATTN DOC CON FOR ROBERT BROWNLEE

LOS ALAMOS SCIENTIFIC LABORATORY
P.O. BOX 1663
LOS, ALAMOS, NM 87545
ATTN DOC CON FOR WILLIAM MAIER

LOS ALAMOS SCIENTIFIC LABORATORY
P.O. BOX 1663
LOS, ALAMOS, NM 87545
ATTN DOC CON FOR JOHN ZINN

LOS ALAMOS SCIENTIFIC LABORATORY
P.O. BOX 1663
LOS, ALAMOS, NM 87545
ATTN DOC CON FOR REFERENCE LIBRARY
ANN BEYER

SANDIA LABORATORIES
LIVERMORE LABORATORY
P.O. BOX 965
LIVERMORE, CA 94556
ATTN DOC CONTROL FOR
THOMAS COOK ORG 8000

SANDIA LABORATORIES
P.O. BOX 5800
ALBUQUERQUE, NM 87115
ATTN DOC CONT. FOR
W.D. BROWN ORG 1353

SANDIA LABORATORIES
P.O. BOX 5800
ALBUQUERQUE, NM 87115
ATTN DOC CONT. FOR
L. ANDERSON ARG 1247

SANDIA LABORATORIES
P.O. BOX 5800
ALBUQUERQUE, NM 87115
ATTN DOC CONT.
FOR MORGAN KRAMMA ORG 5720

SANDIA LABORATORIES
P.O. BOX 5800
ALBUQUERQUE, NM 87115
ATTN DOC CONT.
FOR FRANK HUDSON ORG 1722

SANDIA LABORATORIES
P.O. BOX 5800
ALBUQUERQUE, NM 87115
ATTN DOC CONT.
FOR ORG 3422-1 SANDIA REPTS COLL.

ARGONNE NATIONAL LABORATORY
RECORDS CONTROL
9700 SOUTH CASS AVENUE
ARGONNE, IL 60439
ATTN DOC CON FOR A C WAHL

ARGONNE NATIONAL LABORATORY
RECORDS CONTROL
9700 SOUTH CASS AVENUE
ARGONNE, IL 60439
ATTN DOC CON FOR DAVID W GREEN

ARGONNE NATIONAL LABORATORY
RECORDS CONTROL
9700 SOUTH CASS AVENUE
ARGONNE, IL 60439
ATTN DOC CON FOR LIR SVCS RPTS SEC

ARGONNE NATIONAL LABORATORY
RECORDS CONTROL
9700 SOUTH CASS AVENUE
ARGONNE, IL 60439
ATTN DOC CON FOR S GARELNICK

ARGONNE NATIONAL LABORATORY
RECORDS CONTROL
9700 SOUTH CASS AVENUE
ARGONNE, IL 60439
ATTN DOC CON FOR GERALD T REEDY

UNIVERSITY OF CALIFORNIA
LAWRENCE LIVERMORE LABORATORY
P.O. BOX 808
LIVERMORE CA 94550
ATTN W.H. DUEWER GEN L-404

UNIVERSITY OF CALIFORNIA
LAWRENCE LIVERMORE LABORATORY
P.O. BOX 808
LIVERMORE CA 94550
ATTN JULIUS CHANG L-71

UNIVERSITY OF CALIFORNIA
LAWRENCE LIVERMORE LABORATORY
P.O. BOX 808
LIVERMORE CA 94550
G.R. HAUGEN L-404

UNIVERSITY OF CALIFORNIA
LAWRENCE LIVERMORE LABORATORY
P.O. BOX 808
LIVERMORE CA 94550
ATTN D.J. WUERBLES L-142

CALIFORNIA, STATE OF
AIR RESOURCE BOARD
9528 TELSTA AVE
AL MONTE, CA 91731
ATTN LEO ZAFONTE

CALIFORNIA INSTITUTE OF TECHNOLOGY
JET PROPULSION LABORATORY
4800 OAK GROVE DRIVE
PASADENA CA 91103
ATTN JOSEPH A JELLO

US ENERGY RSCH & DEV ADMIN
DIVISION OF HEADQUARTERS SERVICES
LIBRARY BRANCH G-043
WASHINGTON, DC 20545
ATTN DOC CON FOR CLASS TECH LIB

DEPARTMENT OF TRANSPORTATION
OFFICE OF THE SECRETARY
TAD-44,1, ROOM 10402-R
400 7TH STREET S.W.
WASHINGTON, DC 20590
ATTN SAMUEL C CORONITI

NASA
GODDARD SPACE FLIGHT CENTER
GREENBELT, MD 20771
ATTN A C AIKEN

NASA
GODDARD SPACE FLIGHT CENTER
GREENBELT, MD 20771
ATTN A TEMPKIN

NASA
GODDARD SPACE FLIGHT CENTER
GREENBELT, MD 20771
ATTN A J BAUER

NASA
GODDARD SPACE FLIGHT CENTER
GREENBELT, MD 20771
ATTN TECHNICAL LIBRARY

NASA
GODDARD SPACE FLIGHT CENTER
GREENBELT, MD 20771
ATTN J. SIRY

NASA
600 INDEPENDENCE AVENUE S W
WASHINGTON, DC 20546
ATTN A GESSOW

NASA
600 INDEPENDENCE AVENUE S W
WASHINGTON, DC 20546
ATTN D P CAUFFMAN

NASA
600 INDEPENDENCE AVENUE S W
WASHINGTON, DC 20546
ATTN LTC D R HALLENBECK CODE SG

NASA
600 INDEPENDENCE AVENUE S W
WASHINGTON, DC 20546
ATTN R FELLOWS

NASA
600 INDEPENDENCE AVENUE S W
WASHINGTON, DC 20546
ATTN A SCHARDT

NASA
600 INDEPENDENCE AVENUE S W
WASHINGTON, DC 20546
ATTN M TEPPER

NASA
LANGLEY RESEARCH CENTER
LANGLEY STATION
HAMPTON, VA 23365
ATTN CHARLES SCHEXNAYDER MS-168

NASA
AMES RESCH CENTER
MOFFETT FIELD, CA 94035
ATTN N-254-4 WALTER L. STARR

NASA
AMES RESEARCH CENTER
MOFFETT FIELD, CA 94035
ATTN N-254-4 R WHITTEN

NASA
AMES RESEARCH CENTER
MOFFETT FIELD, CA 94035
ATTN N-254-4 ILIA G POPPOFF

NASA
AMES RESEARCH CENTER
MOFFETT FIELD, CA 94036
ATTN N-254-3 NEIL H FARLOW

NASA
GEORGE C MARSHALL
SPACE FLIGHT CENTER
HUNTSVILLE, AL 35812
ATTN C R BALCHER

NASA
GEORGE C MARSHALL
SPACE FLIGHT CENTER
HUNTSVILLE, AL 35812
ATTN H STONE

NASA
GEORGE C MARSHALL
SPACE FLIGHT CENTER
HUNTSVILLE, AL 35812
ATTN W A ORAN

NASA
GEORGE C MARSHALL
SPACE FLIGHT CENTER
HUNTSVILLE, AL 35812
ATTN CODE ES22 JOHN WATTS

NASA
GEORGE C MARSHALL
SPACE FLIGHT CENTER
HUNTSVILLE, AL 35812
ATTN W T ROBERTS

NASA
GEORGE C MARSHALL
SPACE FLIGHT CENTER
HUNTSVILLE, AL 35812
ATTN R D HUDSON

NASA
GEORGE C MARSHALL
SPACE FLIGHT CENTER
HUNTSVILLE, AL 35812
ATTN R CHAPPELL

ALBANY METALLURGY RESCH CENTER
U S BUREAU OF MINES
P.O. BOX 70
ALBANY, OR 97321
ATTN ELEANOR ARSHIRE

CENTRAL INTELLIGENCE AGENCY
ATTN RD/SI RM 5G48 HQ BLDG
WASHINGTON DC 20505
ATTN NED/OSI-2G4R HQS

DEPARTMENT OF COMMERCE
NATIONAL BUREAU OF STANDARDS
WASHINGTON, DC 20234
ATTN SEC OFFICER FOR
ATTN JAMES DEVOE

DEPARTMENT OF COMMERCE
NATIONAL BUREAU OF STANDARDS
WASHINGTON, DC 20234
ATTN SEC OFFICER
STANLEY ARRAMOWITZ

DEPARTMENT OF COMMERCE
NATIONAL BUREAU OF STANDARDS
WASHINGTON, DC 20234
ATTN SEC OFFICER FOR
ATTN J COOPER

DEPARTMENT OF COMMERCE
NATIONAL BUREAU OF STANDARDS
WASHINGTON, DC 20234
ATTN SEC OFFICER FOR
ATTN GEORGE A SINNATT

DEPARTMENT OF COMMERCE
NATIONAL BUREAU OF STANDARDS
WASHINGTON, DC 20234
ATTN SEC OFFICER FOR
ATTN K KESSLER

DEPARTMENT OF COMMERCE
NATIONAL BUREAU OF STANDARDS
WASHINGTON, DC 20234
ATTN SEC OFFICER FOR
ATTN M KRAUSS

DEPARTMENT OF COMMERCE
NATIONAL BUREAU OF STANDARDS
WASHINGTON, DC 20234
ATTN SEC OFFICER FOR
ATTN LEWIS H GEVANTMAN

DEPARTMENT OF COMMERCE
NATIONAL BUREAU OF STANDARDS
WASHINGTON, DC 20234
ATTN SEC OFFICER FOR
ATTN JAMES DEVOE

NATIONAL OCEANIC & ATMOSPHERIC ADMIN
ENVIRONMENTAL RESEARCH LABORATORIES
DEPARTMENT OF COMMERCE
BOULDER, CO 80302
ATTN GEORGE C REID AERONOMY LAB

NAT OCEANIC & ATMOSPHERIC ADMIN
ENVIRONMENTAL RESEARCH LABORATORIES
DEPARTMENT OF COMMERCE
BOULDER, CO 80302
ATTN ELDON FERGUSON

NAT OCEANIC & ATMOSPHERIC ADMIN
ENVIRONMENTAL RESEARCH LABORATORIES
DEPARTMENT OF COMMERCE
BOULDER, CO 80302
ATTN FRED FEHSENFELD

AERO-CHEM RESCH LABS, INC
P.O. BOX 12
PRINCETON, NJ 08540
ATTN A FONTIJN

AERO-CHEM RESCH LABS, INC
P.O. BOX 12
PARINCETON, NJ 08540
ATTN H PERGAMENT

AERODYNE RESEARCH, INC
BEDFORD RESEARCH PARK
CROSBY DRIVE
BEDFORD, MA 01731 ATTN F BIEN

AERODYNE RESEARCH, INC
BEDFORD RESEARCH PARK
CROSBY DRIVE
BEDFORD, MA 01731 ATTN M CAMAC

AERONOMY CORPORATION
217 S NEIL STREET
CHAMPAIGN, IL 61820
ATTN A BOWHILL

AEROSPACE CORPORATION
P.O. BOX 92957
LOS ANGELES, CA 90009
ATTN N COHEN

AEROSPACE CORPORATION
P.O. BOX 92957
LOS ANGELES, CA 90009
ATTN HARRIS MAYER

AEROSPACE CORPORATION
P.O. BOX 92957
LOS ANGELES, CA 90009
ATTN SIDNEY W KASH

AEROSPACE CORPORATION
P.O. BOX 92957
LOS ANGELES, CA 90009
ATTN T WIDHOPH

AEROSPACE CORPORATION
P.O. BOX 92957
LOS ANGELES, CA 90009
ATTN R J MCNEAL

AEROSPACE CORPORATION
P.O. BOX 92957
LOS ANGELES, CA 90009
ATTN R GROVE

AEROSPACE CORPORATION
P.O. BOX 92957
LOS ANGELES, CA 90009
ATTN IRVING M GARFUNKEL

AEROSPACE CORPORATION
P.O. BOX 92957
LOS ANGELES, CA 90009
ATTN THOMAS D TAYLOR

AEROSPACE CORPORATION
P.O. BOX 92957
LOS ANGELES, CA 90009
ATTN V JOSEPHSON

AEROSPACE CORPORATION
P.O. BOX 92957
LOS ANGELES, CA 90009
ATTN JULIAN REINMEIMER

AEROSPACE CORPORATION
P.O. BOX 92957
LOS ANGELES, CA 90009
ATTN R D RAWCLIFFE

AVCO-EVERETT RESCH LAB INC
2385 REVERE BEACH PARKWAY
EVERETT, MA 02149
ATTN TECHNICAL LIBRARY

AVCO-EVERETT RESCH LAB INC
2385 REVERE BEACH PARKWAY
EVERETT, MA 02149
ATTN GEORGE SUTTON

AVCO-EVERETT RESCH LAB INC
2385 REVERE BEACH PARKWAY
EVERETT, MA 02149
ATTN C W VON ROSENBERG JR

BATTELLE MEMORIAL INSTITUTE
505 KING AVENUE
COLUMBUS, OH 43201
ATTN DONALD J HAMMAN

BATTELLE MEMORIAL INSTITUTE
505 KING AVENUE
COLUMBUS, OH 43201
ATTN DONALD J HAM

BATTELLE MEMORIAL INSTITUTE
505 KING AVENUE
COLUMBUS, OH 43201
ATTN STOIAC

BATTELLE MEMORIAL INSTITUTE
505 KING AVENUE
COLUMBUS, OH 43201
ATTN RICHARD K THATCHER

BROWN ENGINEERING COMPANY INC
CUMMINGS RESCH PARK
HUNTSVILLE, AL 35807
ATTN N PASSINO

THE TRUSTEES OF BOSTON COLLEGE
CHESTNUT HILL CAMPUS
CHESTNUT HILL, MA 02167
ATTN CHAIRMAN DEPT OF CHEM

BROWN ENGINEERING COMPANY INC
CUMMINGS RESEARCH PARK
HUNTSVILLE, AL 35807
ATTN RONALD PATRICK

CALIFORNIA AT RIVERSIDE, UNIV OF
RIVERSIDE, CA 92502
ATTN ALAN C LLOYD

CALIFORNIA AT RIVERSIDE, UNIV OF
RIVERSIDE, CA 92502
ATTN JAMES N PITTS JR

CALIFORNIA AT SAN DIEGO, UNIV OF
3175 MIRAMAR ROAD
LA JOLLA, CA 92037
ATTN S C LIN

CALIFORNIA UNIVERSITY OF
BERKELEY CAMPUS ROOM 318
SPROUL HALL
BERKELEY, CA 94720
ATTN SEC OFFICER FOR HAROLD JOHNSTON

CALIFORNIA UNIVERSITY OF
BERKELEY CAMPUS ROOM 318
SPROUL HALL
BERKELEY, CA 94720
ATTN SEC OFFICER FOR F MOZER

CALIFORNIA UNIVERSITY OF
BERKELEY CAMPUS ROOM 318
SPROUL HALL
BERKELEY, CA 94720
ATTN SEC OFFICER FOR DEPT OF CHAM
W H MILLER

CALIFORNIA, STATE OF
AIR RESOURCES BOARD
9528 TELSTAR AVENUE
EL MONTE, CA 91731
ATTN LEO ZAFONTE

CALSPAN CORPORATION
P.O. BOX 235
BUFFALO, NY 14224
ATTN C E TREANOR

CALSPAN CORPORATION
P.O. BOX 235
BUFFALO, NY 14221
ATTN G C VALLEY

CALSPAN CORPORATION
P.O. BOX 235
BUFFALO, NY 14221
ATTN M G DUNN

CALSPAN CORPORATION
P.O. BOX 235
BUFFALO, NY 14221
ATTN W WURSTER

COLORADO, UNIVERSITY OF
OFFICE OF CONTRACTS AND GRANTS
380 ADMINISTRATIVE ANNEX
BOULDER, CO 80302
ATTN A PHELPS JILA

COLORADO, UNIVERSITY OF
OFFICE OF CONTRACTS AND GRANTS
380 ADMINISTRATIVE ANNEX
BOULDER, CO 80302
ATTN JEFFREY B PEARCE LASP

COLORADO, UNIVERSITY OF
OFFICE OF CONTRACT AND GRANTS
380 ADMINISTRATIVE ANNEX
BOULDER, CO 80302
ATTN C BEATY JILA

COLORADO, UNIVERSITY OF
OFFICE OF CONTRACTS AND GRANTS
380 ADMINISTRATIVE ANNEX
BOULDER, CO 80302
ATTN C LINEBERGER JILA

COLORADO, UNIVERSITY OF
OFFICE OF CONTRACTS AND GRANTS
380 ADMINISTRATIVE ANNEX
BOULDER, CO 80302
ATTN CHARLES A BARTH LASP

COLUMBIA UNIVERSITY, THE TRUSTEES
IN THE CITY OF NEW YORK
LA MONT DOHERTY GEOLOGICAL
OBSERVATORY-TORREY CLIFF
PALISADES, NY 19064
ATTN B PHELAN

COLUMBIA UNIVERSITY, THE TRUSTEES
OF THE CITY OF NEW YORK
116TH STREET & BROADWAY
NEW YORK, NY 10027
ATTN RICHARD N ZARE

COLUMBIA UNIV, THE TRUSTEES OF
CITY OF NEW YORK
116TH & BROADWAY
NEW YORK, NY 10027
ATTN SEC OFFICER H M FOLEY

CONCORD SCIENCES
P.O. BOX 119
CONCORD, MA 01742
ATTN EMMETT A SUTTON

DENVER, UNIVERSITY OF
COLORADO SEMINARY
DENVER RESEARCH INSTITUTE
P.O. BOX 10127 DENVER, CO 80210
ATTN SEC OFFICER FOR MR VAN ZYL

DENVER, UNIVERSITY OF
COLORADO SEMINARY
DENVER RESEARCH INSTITUTE
P.O. BOX 10127 DENVER, CO 80210
ATTN SEC OFFICER FOR DAVID MURCRAE

GENERAL ELECTRIC COMPANY
TEMPO-CENTER FOR ADVANCED STUDIES
816 STATE STREET (P.O. DRAWER QQ)
SANTA BARBARA, CA 93102
ATTN DASAIC

GENERAL ELECTRIC COMPANY
TEMPO-CENTER FOR ADVANCED STUDIES
816 STATE STREET (P.O. DRAWER QQ)
SANTA BARBARA, CA 93102
ATTN WARREN S KNAPP

GENERAL ELECTRIC COMPANY
TEMPO-CENTER FOR ADVANCED STUDIES
816 STATE STREET (P.O. DRAWER)
SANTA BARBARA, CA 93102
ATTN TIM STEPHENS

GENERAL ELECTRIC COMPANY
TEMPO-CENTER FOR ADVANCED STUDIES
816 STATE STREET (P.O. DRAWER QQ)
SANTA BARBARA, CA 93102
ATTN DON CHANDLER

GENERAL ELECTRIC COMPANY
TEMPO-CENTER FOR ADVANCED STUDIES
816 STATE STREET (P.O. DRAWER QQ)
SANTA BARBARA, CA 93102
ATTN B CAMBILL

GENERAL ELEC. CO.
SPACE DIVISION
VALLEY FORGE SPACE CTR
GODDARD BLVD
KING OF PRUSSIA
P.O. BOX 8555
PHILADELPHIA, PA 19101
ATTN M H BORTNER, SPACE SCIENCE LAB

GENERAL ELEC. CO.
SPACE DIVISION
VALLEY FORGE SPACE CENTER
GODDARD BLVD. KING OF PRUSSIA
P.O. BOX 8555
PHILADELPHIA, PA 19101
ATTN J BURNS

GENERAL ELEC. CO.
SPACE DIVISION
VALLEY FORGE SPACE CENTER
GODDARD BLVD KING OF PRUSSIA
P.O. BOX 8555
PHILADELPHIA, PA 19101
ATTN F ALYEA

GENERAL ELEC. CO.
SPACE DIVISION
VALLEY FORGE SPACE CENTER
GODDARD BLVD KING OF PRUSSIA
P.O. BOX 8555
PHILADELPHIA, PA 19101
ATTN P ZAVITSANDS

GENERAL ELEC. CO.
SPACE DIVISION
VALLEY FORGE SPACE CENTER
GODDARD BLVD KING OF PRUSSIA
P.O. BOX 8555
PHILADELPHIA, PA 19101
ATTN R H EDSALL

GENERAL ELEC. CO.
SPACE DIVISION
VALLEY FORGE SPACE CENTER
GODDARD BLVD KING OF PRUSSIA
P.O. BOX 8555
PHILADELPHIA, PA 19101
ATTN T BAURER

GENERAL RESEARCH CORPORATION
P.O. BOX 3587
SANTA BARBARA, CA 93105
ATTN JOHN ISE JR

GEOPHYSICAL INSTITUTE
UNIVERSITY OF ALASKA
FAIRBANKS, AK 99701
ATTN D HENDERSON

GEOPHYSICAL INSTITUTE
UNIVERSITY OF ALASKA
FAIRBANKS, AK 99701
ATTN J S WAGNER PHYSICS DEPT

GEOPHYSICAL INSTITUTE
UNIVERSITY OF ALASKA
FAIRBANKS, AK 99701
ATTN B J WATKINS

GEOPHYSICAL INSTITUTE
UNIVERSITY OF ALASKA
FAIRBANKS, AK 99701
ATTN T N DAVIS

GEOPHYSICAL INSTITUTE
UNIVERSITY OF ALASKA
FAIRBANKS, AK 99701
ATTN R PARTHASARATHY

GEOPHYSICAL INSTITUTE
UNIVERSITY OF ALASKA
FAIRBANKS, AK 99701
ATTN NEAL BROWN

LOWELL, UNIVERSITY OF
CENTER FOR ATMOSPHERIC RESEARCH
450 AIKEN STREET
LOWELL, MA 01854
ATTN G T BEST

LOCKHEED MISSILES & SPACE COMPANY
3251 HANOVER STREET
PALO ALTO, CA 94394
ATTN JOHN KUMER DEPT 52-54

LOCKHEED MISSILES & SPACE COMPANY
3251 HANOVER STREET
PALO, ALTO, CA 94304
ATTN KIMER DEPT 52-54

LOCKHEED MISSILES & SPACE COMPANY
3251 HANOVER STREET
PALO, ALTO, CA 94304
ATTN JOHN B CLADIS DEPT 52-12

LOCK HEED MISSILES & SPACE CO
3251 HANOVER STREET
PALO, ALTO, CA 94304
ATTN GILLY M MCCORMAC DEPT 52-54

LOCKHEED MISSILES & SPACE CO
3251 HANOVER STREET
PALO, ALTO, CA 94304
ATTN TOM JAMES DEPT 52-54

LOCKHEED MISSILES & SPACE CO
3251 HANOVER STREET
PALO, ALTO, CA 94304
ATTN J B REAGAN D/52-12

LOCKHEED MISSILES & SPACE CO
3251 HANOVER STREET
PALO, ALTO, CA 94304
ATTN MARTIN WALT DEPT 52-10

LOCKHEED MISSILES & SPACE CO
3251 HANOVER STREET
PALO, ALTO, CA 94304
ATTN RICHARD G JOHNSON DEPT 52-12

LOCKHEED MISSILES & SPACE CO
3251 HANOVER STREET
PALO, ALTO, CA 94304
ATTN ROBERT D SEARS DEPT 52-14

LOCKHEED MISSILES & SPACE CO
3251 HANOVER STREET
PALO, ALTO, CA 94304
ATTN J R WINKLER

INSTITUTE FOR DEFENSE ANALYSE
400 ARMY-NAVY DRIVE
ARLINGTON, VA 22202
ATTN ERNEST GAUER

INSTITUTE FOR DEFENSE ANALYSE
400 ARMY-NAVY DRIVE
ARLINGTON, VA 22202
ATTN HANS WOLFARD

MISSION RESEARCH CORPORATION
735 STATE STREET
SANTA BARBARA, CA 93101
ATTN D ARCHER

MISSION RESEARCH CORPORATION
735 STATE STREET
SANTA BARBARA, CA 93101
ATTN D FISCHER

MISSION RESEARCH CORPORATION
735 STATE STREET
SANTA BARBARA, CA 93101
ATTN M SCHEIBE

MISSION RESEARCH CORPORATION
735 STATE STREET
SANTA BARBARA, CA 93101
ATTN D SAPPENFIELD

MISSION RESEARCH CORPORATION
735 STATE STREET
SANTA BARBARA, CA 93101
ATTN D SOWLE

PHOTOMETRIC, INC.
442 MARETT ROAD
LEXINGTON, MA 02173
ATTN IRVING L KOFSKY

PHYSICAL DYNAMICS INC.
P.O. BOX 1069
BERKELEY, CA 94701
ATTN J B WORKMAN

PHYSICAL DYNAMICS INC.
P.O. BOX 1069
BERKELEY, CA 94701
ATTN A THOMPSON

PHYSICAL SCIENCES, INC.
30 COMMERCE WAY
WOBBURN, MA 01801
ATTN KURT WRAY

PHYSICAL SCIENCES, INC.
30 COMMERCE WAY
WOBBURN, MA 01801
ATTN R L TAYLOR

PHYSICAL SCIENCES, INC.
30 COMMERCE WAY
WOBBURN, MA 01801
ATTN G CALEDONIA

PHYSICS INTERNATIONAL COMPANY
2700 MERCED STREET
SAN LEANDRO, CA 94577
ATTN DOC CON FOR TECH LIB

PITTSBURGH, UNIV OF
OF THE COMWLTH SYS OF HIGHER EDUC
CATHEDRAL OF LEARNING
PITTSBURGH, PA 15213
ATTN WADE L FITE

PITTSBURGH, UNIVERSITY OF
OF THE COMWLTH SYS OF HIGHER EDUC
CATHEDRAL OF LEARNING
PITTSBURGH, PA 15213
ATTN MANFRED A BIONDI

PITTSBURGH, UNIVERSITY OF
OF THE COMWLTH SYS OF HIGHER EDUC
CATHEDRAL OF LEARNING
PITTSBURGH, PA 15213
ATTN FREDERICK KAUFMAN

PITTSBURGH, UNIVERSITY OF
OF THE COMWLTH SYS OF HIGHER EDUC
CATHEDRAL OF LEARNING
PITTSBURGH, PA 15213
ATTN EDWARD GERJUOY

PRINCETON UNIV, THE TRUSTEES OF
FORRESTAL CAMPUS LIBRARY
BOX 710
PRINCETON UNIVERSITY
PRINCETON, NJ 08540
ATTN ARNOLD J KELLY

R & D ASSOCIATES
P.O. BOX 9695
MARINA DEL REY, CA 90291
ATTN RICHARD LATTER

R & D ASSOCIATES
P.O. BOX 9695
MARINA DEL REY, CA 90291
ATTN R G LINDGREN

R & D ASSOCIATES
P.O. BOX 9695
MARINA DEL REY, CA 90291
ATTN BRYAN GABBARD

R & D ASSOCIATES
P.O. BOX 9695
MARINA DEL REY, CA 90291
ATTN H A DRY

R & D ASSOCIATES
P.O. BOX 9695
MARINA DEL REY, CA 90291
ATTN ROBERT E LELEVIER

R & D ASSOCIATES
P.O. BOX 9695
MARINA DEL REY, CA 90291
ATTN R P TURCO

R & D ASSOCIATES
P.O. BOX 9695
MARINA DEL REY, CA 90291
ATTN ALBERT L LATTER

R & D ASSOCIATES
P.O. BOX 9695
MARINA DEL REY, CA 90291
ATTN FORREST GILMORE

R & D ASSOCIATES
P.O. BOX 9695
MARINA DEL REY, CA 90291
ATTN D DEE

R & D ASSOCIATES
1815 N. FT. MYER DRIVE
11TH FLOOR
ARLINGTON, VA 22209
ATTN HERBERT J MITCHELL

R & D ASSOCIATES
1815 N. FT. MYER DRIVE
11TH FLOOR
ARLINGTON, VA 22209
ATTN J W ROSENGREN

RAND CORPORATION
1700 MAIN STREET
SANTA MONICA, CA 90406
ATTN CULLEN CRAIN

SCIENCE APPLICATIONS, INC.
P.O. BOX 2351
LA JOLLA, CA 92038
ATTN DANIEL A HAMLIN

SCIENCE APPLICATIONS, INC.
P.O. BOX 2351
LA JOLLA, CA 92038
ATTN DAVID SACHS

SPACE DATA CORPORATION
1331 SOUTH 26TH STREET
PHOENIX, AZ 85034
ATTN EDWARD F ALLEN

STANFORD RSCH INSTITUTE INTERNATIONAL
333 RAVENSWOOD AVENUE
MENLO PARK, CA 94025
ATTN M BARON

STANFORD RSCH INSTITUTE INTL
333 RAVENSWOOD AVENUE
MENLO PARK, CA 94025
ATTN L LEADABRAND

STANFORD RSCH INSTITUTE INTL
333 RAVENSWOOD AVENUE
MENLO PARK, CA 94025
ATTN WALTER H CHESTNUT

STANFORD RSCH INSTITUTE INTL
1611 NORTH KENT STREET
ARLINGTON, VA 22209
ATTN WARREN W BERNING

STANFORD RSCH INSTITUTE INTL
1611 NORTH KENT STREET
ARLINGTON, VA 22209
ATTN CHARLES HULBERT

TECHNOLOGY INTL CORPORATION
75 WIGGINS AVENUE
BEDFORD, MA 01730
ATTN W P BOQUIST

UNITED TECHNOLOGIES CORP
755 MAIN STREET
HARTFORD, CT 06103
ATTN H MICHELS

UNITED TECHNOLOGIES CORP
755 MAIN STREET
HARTFORD, CT 06103
ATTN ROBERT HBULLIS

UTAH STATE UNIVERSITY
LOGAN, UT 84321
ATTN DORAN BAKER

UTAH STATE UNIVERSITY
LOGAN, UT 84321
ATTN KAY BAKER

UTAH STATE UNIVERSITY
LOGAN, UT 84321
ATTN C WYATT

UTAH STATE UNIVERSITY
LOGAN, UT 84321
ATTN D BURT

VISIDYNE, INC.
19 THIRD AVENUE
NORTHWEST INDUSTRIAL PARK
BURLINGTON, MA 01803
ATTN HENRY J SMITH

VISIDYNE, INC.
19 THIRD AVENUE
NORTHWEST INDUSTRIAL PARK
BURLINGTON, MA 01803
ATTN J W CARPENTER

VISIDYNE, IND.
19 THIRD AVENUE
NORTHWEST INDUSTRIAL PARK
BURLINGTON, MA 01803
ATTN WILLIAM REIDY

VISIDYNE, INC.
19 THIRD AVENUE
NORTHWEST INDUSTRIAL PARK
BURLINGTON, MA 01803
ATTN T C DEGGES

VISIDYNE, INC.
19 THIRD AVENUE
NORTHWEST INDUSTRIAL PARK
BURLINGTON, MA 01803
ATTN CHARLES HUMPHREY

WAYNE STATE UNIVERSITY
1064 MACKENZIE HALL
DETROIT, MI 48202
ATTN PIETER K ROL
CHAM ENGR & MAT SCI

WAYNE STATE UNIVERSITY
1064 MACKENZIE HALL
DETROIT, MI 48202
ATTN R H KUMMLER

WAYNE STATE UNIVERSITY
DEPT. OF PHYSICS
DETROIT, MI 48202
ATTN WALTER E KAUPPILA

YALE UNIVERSITY
NEW HAVEN, CT 06520
ATTN ENGINEERING DEPARTMENT